Real-time 3D MR-Thermometry using a Stack-of-Stars Gradient Echo Pulse Sequence

BSc Thesis Biomedical Engineering

Elke Putman
S2624257

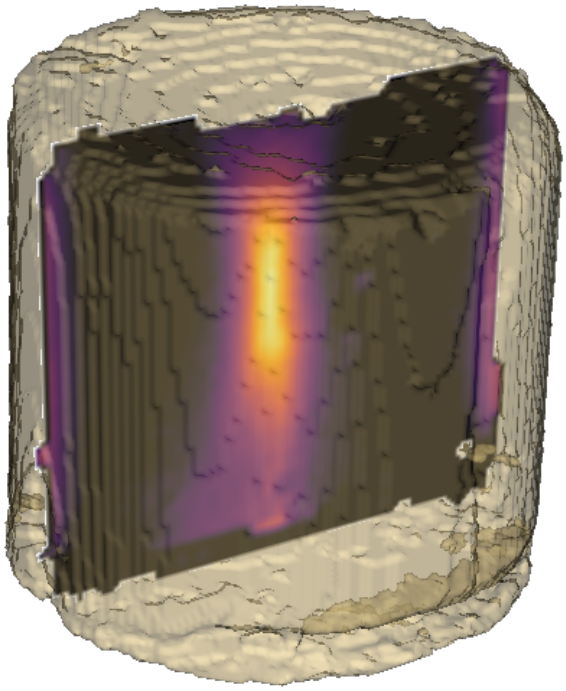

Supervisors:
Prof.dr.ir. B. ten Haken (Bernard)
Dr. ir. W.M. Brink (Wyger)
Ir. J.L. van der Hoek (Jan)

University of Twente
Magnetic Detection & Imaging
Faculty of Science & Technology
November 22, 2023

ABSTRACT

Introduction: Thermal ablation is a minimally invasive technique in the treatment of tumors. Accurate temperature monitoring in tissue is crucial for ensuring patient safety and the efficacy of the treatment. MR-thermometry is a commonly used method for temperature monitoring. Real-time application of this method operates mainly in 2D due to the low temporal resolution of MRI. 3D temperature monitoring would be preferable for better volumetric coverage of heated regions, thereby improving patient safety. The 3D Stack-of-Stars Gradient Echo pulse sequence (3D-RAVE) could be a robust option, offering a flexible spatiotemporal resolution for monitoring temperature during an ablation procedure. The aim of this study is to evaluate the temperature accuracy of the 3D-RAVE in combination with a model-based reconstruction approach for temperature determination. Additionally, it will be determined at what acceleration factor reliable temperature maps can be acquired.
Methods: A phantom made of 2% agar heated to a temperature of approximately 14.5 °C with high-intensity focused ultrasound. During ablation, a dataset is recorded with the 3D-RAVE sequence. Also, the temperature change is followed in real-time with a fiber optic sensor. Temperature maps were reconstructed using both the model-based reconstruction method and a conventional reconstruction method. These temperature maps were compared to each other and to the sensor temperature to evaluate the temperature accuracy of the 3D-RAVE sequence. Additionally, temperature maps were reconstructed using undersampled data and based on an error analysis, a maximal acceleration factor was determined.
Results: The 2D-EPI sequence contains a deviation of approximately 1.5 °C of the sensor temperature, whereas the 3D-RAVE sequence demonstrated a 0.5 °C deviation. Error analysis of undersampled data revealed an increasing error trend with fewer spokes, with an $\pm$ 1 °C error observed for 64 spokes.
Conclusion: The 3D Stack-of-Stars Gradient Echo pulse sequence is, when fully sampled, capable of determining the temperature change during an ablation procedure. For real-time temperature monitoring, reliable temperature maps can be created with a minimum of 64 spokes although there is potential for improvement in temperature accuracy.

SAMENVATTING

Inleiding: Thermische ablatie is een minimaal invasieve techniek bij de behandeling van tumoren. Nauwkeurige temperatuurmonitoring in weefsel is essentieel om de veiligheid van de patiënt en de effectiviteit van de behandeling te verzekeren. MR-thermometrie is een veelgebruikte methode voor temperatuurmonitoring. De real-time toepassing van deze methode wordt voornamelijk uigevoerd in 2D. 3D-temperatuurmonitoring zou de voorkeur hebben omdat dit zorgt voor een betere volumetrische weergave van verhitte gebieden, wat de veiligheid van de patiënt verbetert.
De 3D Stack-of-Stars Gradient Echo-pulssequentie (3D-RAVE) kan een robuuste optie zijn, met een flexibele ruimtelijke en temporele resolutie voor het monitoren van de temperatuur tijdens een ablatieprocedure. Het doel van dit onderzoek is het evalueren van de temperatuurnauwkeurigheid van 3D-RAVE in combinatie met een model-based reconstructie methode. Daarnaast zal bepaald worden met welke versnellingsfactor nog steeds betrouwbare temperatuur afbeeldingen te verkrijgen zijn.
Methode: Een fantoom gemaakt van 2% Agar werd geableerd met high-intensity focused ultrasound. Voor en na de ablatie werden k-space-datasets opgenomen met behulp van de 3D-RAVE- en 2D-EPI-sequenties. Tijdens de ablatie werd een dataset opgenomen met de 3D-RAVE-sequentie. Ook werd de verandering in temperatuur in real-time gevolgd met een optische sensor. Temperatuur afbeeldingen werden gereconstrueerd met zowel de model-based reconstructiemethode als een conventionele reconstructiemethode. Deze temperatuurafbeeldingen werden met elkaar en met de sensortemperatuur vergeleken om de temperatuur nauwkeurigheid van de 3D-RAVE-sequentie te evalueren. Daarnaast werden temperatuur afbeeldingen gereconstrueerd met datasets waar minder data is gebruik. Op basis van een foutenanalyse werd de maximale versnellingsfactor bepaald.
Resultaten: De 2D-EPI-sequentie bevatte een afwijking van ongeveer 1,5°C ten opzichte van de sensortemperatuur, terwijl de 3D-RAVE-sequentie een afwijking van 0,5°C vertoonde. Uit de foutenanalyse van niet volledig gesamplede data bleek dat bij minder data een toenemende fout ontstond, waarbij een $\pm$ 1°C fout werd waargenomen voor 64 spaken.
Conclusie: De 3D Stack-of-Stars Gradient Echo-pulssequentie is, wanneer volledig gesampled, in staat om de verandering in temperatuur tijdens een ablatieprocedure te meten. Voor real-time temperatuurmonitoring kunnen temperatuur afbeeldingen worden gemaakt met een minimum van 64 spaken, hoewel er aanzienlijke ruimte is voor verbetering van de nauwkeurigheid van de temperatuur.

CONTENTS

1 INTRODUCTION

In recent years, the use of image-guided interventions for treating tumors has rapidly grown. One of those interventions is thermal ablation. This is a technique used to treat tumors and is less expensive and minimally invasive alternative to surgical removal. The definition of thermal ablation, given by Brace, runs as follows: ”Thermal ablation refers to the destruction of tissue by extreme hyperthermia or hypothermia.”[1] Various ablation modalities, including radiofrequency (RF) ablation, microwave (MW) ablation, laser ablation and high-intensity focused ultrasound (HIFU) ablation are currently employed in clinical settings. The underlying physical principle of these ablation techniques is to deliver sufficient energy to the targeted tissue in order to induce cellular necrosis. The majority of thermal ablation systems consist of a generator and a needlelike device which is placed near the tumor. HIFU ablation is an exception to this, as it is possible to perform ablation completely non-invasive, using a specialized ultrasound probe. The choice of the ablation approach for a certain patient depends on the type of the tumor, the anatomic location, physician’s preference and the underlying health of the patient.[1, 2] In this study, HIFU ablation will be used to induce heating in a phantom.

During thermal ablation treatment, real-time monitoring of the temperature distribution is crucial. This monitoring prevents damage to healthy tissue surrounding the tumor or in the far fields of HIFU transducers. It also allows measurement of the thermal dose delivered to the targeted tissue. This thermal dose is an important parameter in assessing the impact of the ablation procedure on the tissues. Due to the possibility of detecting temperature changes, MRI appeared to be the ideal modality for temperature monitoring during ablation therapy. There are different MRI parameters that give insight into the temperature change, such as T1 or T2 relaxation of water protons, proton density, diffusion coefficient, and proton resonance frequency (PRF) shift of water protons.[3] Because of its independence of tissue type (except for adipose tissue) and its linearity over the temperature range of interest, PRF is the most widely chosen method for monitoring thermal ablation.[4, 5] In Section 2.3, the principle of PRF shift will be explained in detail.

Obtaining temperature maps by PRF shift depends on the existence of phase changes in images. This brings some difficulties because phase is not only induced due to temperature change but also by spatial field drift or motion. Therefore Grissom et al. developed a method that removes these unwanted contributions.[4] In addition to this model, Gaur et al. developed the k-space hybrid model for temperature map estimation, where temperature change can be calculated directly from k-space samples, instead of the need to reconstruct an image before the temperature calculation.[6]. This last model makes accelerating the image acquisition and reconstruction possible, resulting in an increased frame rate. A further explanation of both models is given in Section 2.4.

HIFU ablation can cause rapid tissue heating, faster than 1°C/s, in a very localized region. Hence, it is important to monitor the temperature distribution over the tissues and the thermal dose at high spatial and temporal resolution. Monitoring ablation therapy is nowadays mostly done using phase-sensitive two-dimensional Fourier transform (2DFT) gradient-recalled echo pulse sequences. Standard 3D sequences are more time-consuming, with acquisition times from 30 seconds up to several minutes, leading to lower temporal resolution.[7, 8] However, 3D temperature monitoring offers distinct advantages compared to 2D monitoring.

Since tumor ablation is a 3D process, single-slice 2D temperature monitoring can cause heating to be missed due to restricted volume coverage. By adopting 3D temperature monitoring, a larger volume coverage and accurate representation of the thermal changes within the tissue can be achieved, leading to improved treatment precision and patient safety. Also, 3D temperature monitoring ensures that the maximum recorded temperature is actually the maximum temperature. Additionally, 2D temperature monitoring may introduce partial volume effects, due to thicker slices, which causes temperature underestimation.[8] Therefore, a 3D MRI sequence with high spatiotemporal resolution would be desired for temperature monitoring during HIFU ablation.

The purpose of this study is to evaluate the potential of performing MR thermometry using a 3D Golden-Angle radial MR sequence together with the aforementioned k-space hybrid method. These reconstructions will be compared to standard 2DFT temperature maps. Because the k-space hybrid method makes it possible to increase the frame rate by undersampling the k-space, it will also be investigated at which maximum acceleration factor valid temperature maps are reconstructed using a 3D Stack-of-Stars Gradient-Echo sampling. This acceleration factor is determined by the amount of recorded data used for image reconstruction. This leads to the following research question: *What is the accuracy of the 3D temperature maps obtained using 3D Stack-of-Stars Gradient Echo sequence and the k-space hybrid model, and what is the maximum acceleration factor for obtaining reliable temperature maps?*

2 BACKGROUND

2.1 Thermal ablation

Thermal ablation can be categorized into different temperature regimes. The first regime exists in the temperature range between 41-46 °C. Within this range, minor cell damage is possible when the tissue is heated for more than ten minutes. To reduce the time needed to acquire cell death, temperatures inside the 46-52 °C range must be used. In this regime, microvascular thrombosis, ischemia, and hypoxia occur. Those processes cause an interruption of the nutrient supply and lead to delayed necrosis. The last regime contains temperatures above 60 °C. Those high temperatures cause rapid protein denaturation and plasma membrane melting. Therefore, temperatures above 60°C will induce rapid necrosis.[1]

2.2 High-intensity focused ultrasound ablation

High-intensity focused ultrasound (HIFU) ablation is one of the procedures to perform thermal ablation. The principle of HIFU ablation is based on heat generation due to the absorption of acoustic energy in the tissue. With a HIFU system, high-intensity acoustic waves, in the range of 100-10000 W/cm^2, are delivered to a focal region with sizes of 1 mm in diameter and about 10 mm in length. For heat generation, frequencies near 1 MHz are considered the most useful. Because energy is delivered from outside the body, HIFU ablation is entirely non-invasive.[9] In Figure 2.1 an example of an MR-guided HIFU ablation treatment is shown. The patient is positioned on the MRI table and the HIFU transducer is positioned in such way that a focus can be created in the tumor. In this case, the HIFU transducer is embedded in the MRI table. The coupling pad and the degassed water make sure that the patient is coupled to the transducer and that acoustic waves are not attenuated by air.[10]

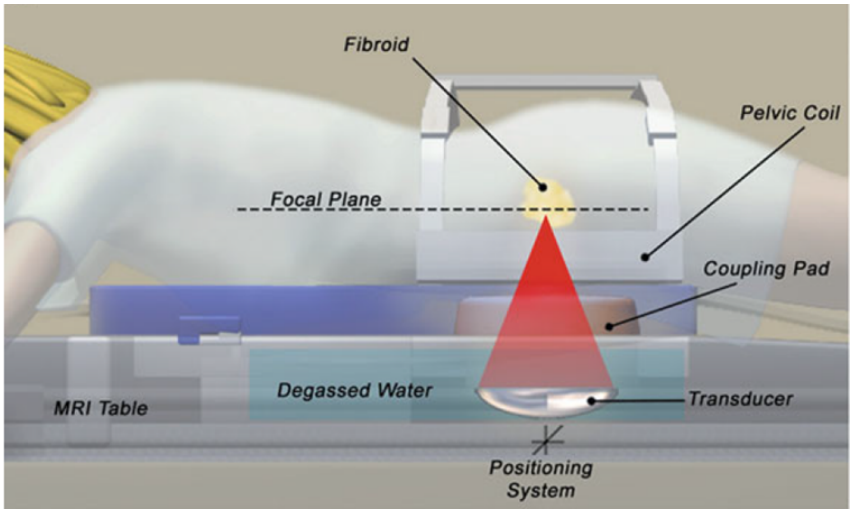

Fig. 2.1: Example of an MR-guided HIFU ablation treatment. The patient is positioned on the MRI table where, in this case the transducer is embedded in the table. With the transducer, a focus is created in the tumor. [10]

2.3 Proton resonance frequency shift

As stated in Chapter 1, the most widely used temperature mapping method for ablation therapy is PRF shift. The fundamental principle of PRF is the fact that the local magnetic field, experienced by a nucleus, is slightly lower than the B_0 field due to shielding. The local field is given by [3]:

$$B_{loc} = B_0 - B_{0s} = (1 - s)B_0 \tag{2.1}$$

Where s denotes the shielding constant. Shielding arises because of electron movement in atomic orbitals which induces a small magnetic field opposing the B_0 field.[11] The lower local magnetic field creates a change in the resonance frequency which now becomes [3]:

$$\omega = \gamma B_{loc} = \gamma B_0(1 - s) \tag{2.2}$$

Where ω is the resonance frequency and γ is the gyromagnetic ratio of an ^1H nucleus ($267.52\ 10^6$ rad s^{-1} T^{-1}). Within a H_2O molecule, the ^1H nucleus is shielded more when the molecule is unbounded than a nucleus within a hydrogen-bonded molecule. As temperature increases there will be less bonding since bonds break. This ensures more shielding, and thus a lower PRF. The shielding component changes linearly with the temperature as follows:

$$s(T) = \alpha T \tag{2.3}$$

Where α is the PRF change coefficient. In aqueous tissue $\alpha = -0.01$ ppm/°C.[4] By measuring the phase change resulting from the change in PRF, the temperature difference between images can be computed by applying the following Equation.

$$\Delta T = \frac{\phi(T) - \phi(T_0)}{\gamma \alpha B_0 [TE]} \tag{2.4}$$

Here $\phi(T)$ denotes the phase in the current image and $\phi(T_0)$ is the phase of a reference image. In case of heating, a negative phase shift is expected. γ is the gyromagnetic ratio of an ^1H nucleus ($267.52\ 10^6$ rad s^{-1} T^{-1}), B_0 denotes the static magnetic field and [TE] is the echo time of a gradient echo pulse sequence.[3]

Figure 2.2 illustrates a PRF temperature map of a brain tumor directly after (laser) ablation. Here, the temperature change map is already converted to an absolute temperature map, where $T = \Delta T + 37$. It is clear to see that a certain region in the brain, in this case the tumor, is heated. The temperature distribution shows the highest temperature at the center of the region. As one moves away from the center, the temperature decreases. In unaffected areas of the brain, the temperature remains 37.0 °C, indicating no heating. These temperature maps provide valuable insights for medical professionals, enabling them to verify whether the targeted region has reached the intended temperature for optimal treatment outcomes.

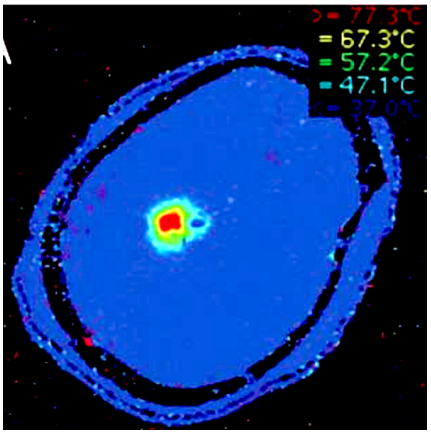

Fig. 2.2: PRF temperature map of a brain tumor directly after ablation.[12]

2.4 Hybrid thermometry models

To separate temperature-induced phase changes from phase changes by other sources like phase variations imposed by the transmit and receive coil, spatial field drift or motion, Grissom et al. developed an image-based method to reconstruct temperature maps.[4] The signal model for image voxel j is shown in Eq. (2.5).

$$y_j = \boldsymbol{W} e^{i(\{\boldsymbol{A}c\}_j + \theta_j)} \tag{2.5}$$

In this formulation, $\boldsymbol{W}$ represents a complex baseline image acquired before heating by fully sampling the k-space. This image contains the (static) phase variations caused by static field inhomogeneities and the transmit and receive coils. $\boldsymbol{A}c$ represents a linear combination of smooth basis functions that vary gradually in space, such as those caused by respiration and center frequency drift. θ is the localized phase shift resulting from the ablation procedure, which is our parameter of interest.

This model is further extended to a k-space signal model by Gaur et al.[6] Also called the k-space hybrid method. In essence, the k-space model is the discrete Fourier transform of the hybrid model in Eq. (2.5), as can be seen in Eq. (2.6).

$$y_i = \sum_{j=1}^{N_s} e^{\iota \vec{k_i} \cdot \vec{x} j} \boldsymbol{W} e^{\iota(\{\boldsymbol{A}c\}_j + \theta_j)} \tag{2.6}$$

With this model, the temperature can be calculated directly from k-space without the need to reconstruct an image before the temperature calculation. In this case, y_i is one k-space data sample and N_s is the number of image voxels.[6] The θ can be estimated by fitting the model in Eq. (2.6) to acquired k-space data by solving the constrained minimization problem shown in Eq. (2.7). This equation incorporates the principle that temperature increase only occurs in a minority of voxels during HIFU ablation. As a result, the sparsity of θ is used as a key factor in the estimation process.

$$\begin{aligned} \text{minimize} \quad & \frac{1}{2}\|\tilde{\boldsymbol{y}} - \boldsymbol{y}(\boldsymbol{c}, \boldsymbol{\theta})\|^2 + \lambda \|\boldsymbol{\theta}\|_1, \\ \text{subject to} \quad & \boldsymbol{\theta} \leqslant 0, \end{aligned} \tag{2.7}$$

The first term in this equation represents the deviation of the modelled data to the measured data. $\tilde{\boldsymbol{y}}$ represents the acquired k-space data and $\boldsymbol{y}(\boldsymbol{c}, \boldsymbol{\theta})$ the modelled data. $\|\boldsymbol{\theta}\|_1$ is the l_1 norm of θ and λ controls the sparsity of θ. A solution of Eq. (2.7) is found by using a minimization algorithm that updates $\boldsymbol{c}$ and $\boldsymbol{\theta}$. The minimization problem can be further extended to Eq. (2.8)

$$\begin{aligned} \text{minimize} \quad & \frac{1}{2}\|\tilde{\boldsymbol{y}} - \boldsymbol{G} diag\{e^{i\theta_j}\}\boldsymbol{f}\|^2 - \lambda \sum_{j=1}^{N_s} \boldsymbol{\theta}_j, \\ \text{subject to} \quad & \boldsymbol{\theta} \leqslant 0, \end{aligned} \tag{2.8}$$

Here, $\boldsymbol{G}$ is a nonuniform discrete Fourier transform matrix and $\boldsymbol{f} \triangleq e^{i\{\boldsymbol{A}\boldsymbol{c}\}_j}\{\boldsymbol{B}\boldsymbol{w}\}$ where $\boldsymbol{B}$ contains the baseline image. $\sum_{j=1}^{N_s} \boldsymbol{\theta}_j$ is the l_1 norm of θ. This minimization problem is solved using a nonlinear conjugate gradient algorithm described in Ref. [6]. The algorithm iterates several times over this minimization problem to update θ and $\boldsymbol{c}$ until the stopping criterion is met. The last step in the algorithm is controlling the sparsity of θ by applying l_1 regularization. The θ and $\boldsymbol{c}$ update steps are repeated with $\lambda = 0$. θ is only updated in voxels with lower values than a certain threshold value. The final θ matrix enables the calculation of temperature changes in all the voxels by Eq. (2.4) where $\phi(T)_j - \phi(T_0)_j = \theta_j$.

The great advantage of the k-space hybrid model is the fact that k-space can be undersampled since baseline images used in the model contain fully sampled k-space data. Therefore aliased images are removable from the solution space.[6] Radial data is fully sampled when more than $\frac{\pi}{2} \cdot n$ spokes are used for an image with n sample points per spoke.[13] This ensures that the Nyquist criterion is met. The derivation of this formula can be found in Appendix A. In the image-based model, it is also possible to use undersampled k-space data but in this case, the undersampling needs to be addressed through conventional image reconstruction approaches. For example, CG-SENSE in combination with the first model can be used to form temperature maps.[7]

2.5 Golden-Angle Radial sampling

Golden-Angle Radial sampling has become a popular sampling trajectory in recent years. Radial sequences have quite some advantages for use in thermometry. Radial sampled images do not have severe wrap-around artifacts due to undersampling. Instead, undersampling-induced artifacts look like added noise.[14] Within radial sampling, the center of k-space, containing most of the dynamic image contrast, is sampled each repetition time (TR). Therefore radial sampling allows a higher frame rate.[8]. Compared to linear radial sampling, the golden angle trajectory makes use of the golden ratio (GR) of 1.618 to determine the angle between consecutive spokes to cover the k-space.[14] The derivation of the golden ratio can be found in Ref. [14]. The Golden-Angle sampling method used in this study is the full-spoke Golden-Angle Radial Sampling. In this case, each spoke is drawn from one side to the other side, therefore the spokes only need to be rotated 180°to cover the entire circle. The golden angle for full-spoke Golden-Angle Radial Sampling is given by:

$$GA = \frac{180^\circ}{GR} \approx \frac{180^\circ}{1.618} \approx 111.25^\circ \tag{2.9}$$

In Figure 2.3 the full-spoke golden angle trajectory as well as a linear radial sampling trajectory are shown. It can be seen that for the golden angle sampling the *n*th spoke always fills the largest gap available. The spokes of the GA sampling never repeat each other which provides good temporal incoherence and is therefore well suited for dynamic MRI applications.[14]

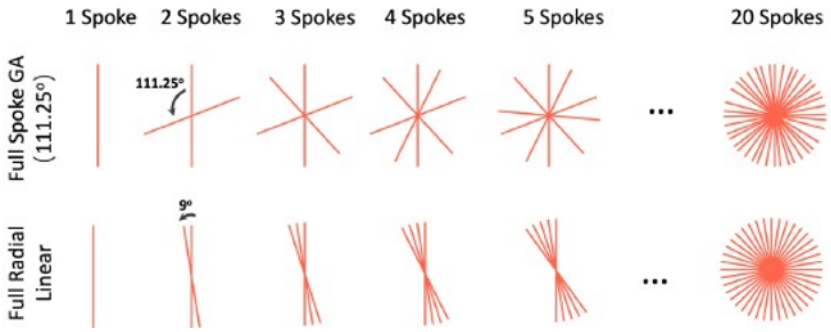

Fig. 2.3: (a,b) Example of full-spoke golden angle trajectory, where each spoke rotates by 111.25°and a linear radial sampling trajectory where each spoke rotates by 180°/20 = 9°.[14]

With Golden-Angle Radial sampling it is also possible to sample k-space in 3D. A way to accomplish this is the Stack-of-Stars Golden-Angle Radial Sampling. Here, the radial sampling takes place in the k_x-k_y plane and in the k_z direction cartesian sampling is applied. In Figure 2.4 the idea of the Stack-of-Stars method is shown.

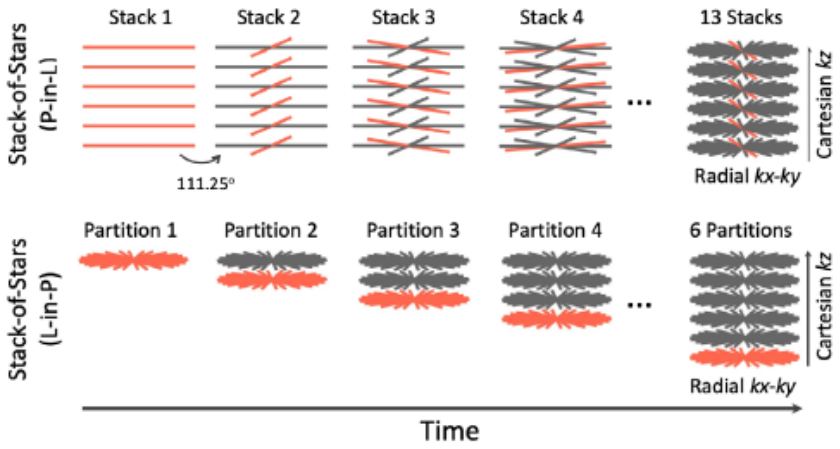

Fig. 2.4: Two procedures for the Stack-of-Stars sampling. The upper row contains the P-in-L. All k_z-locations are sampled at one orientation before moving to the next angle. The L-in-P scheme collects all radial spoke at one k_z-location before the second k_z-location is sampled.[14]

There are two ways of applying the Stack-of-Stars method. In both methods, multiple radial sampled k_x-k_y planes are stacked on top of each other in kz direction. The difference lies in the way the k-spaces are filled. The upper row of Figure 2.4 shows the partition in line (P-in-L) method. Here all the locations in k_z are sampled with a certain angle before the second angle is sampled. The lower row contains the line in partition (L-in-P) method. This procedure first collects all radial spokes at one k_z-location, according to the Golden-Angle sampling, before moving to the next k_z-location.

3 METHODS

3.1 Ring experiment

Prior to an actual HIFU ablation experiment, an experiment with a metal ring is performed to prepare the temperature map reconstruction for the ablation experiment. This ring induces static phase changes due to susceptibility artifacts. These phase shifts can be treated as if they represent static temperature changes. The experimental setup consisted of a Siemens MAGNETOM Aera 1.5T scanner, a 16-channel head coil, a copper-sulfate phantom, and a small metal ring. The metal ring is placed on top of the phantom. Two pulse sequences were used to record the images: a 3D-Gradient Echo (GRE) and a 3D-Stack-of-Stars Gradient Echo, also known as 3D-RAVE, where the P-in-L stacking is employed. The settings of both sequences are shown in Table 3.1.

Table 3.1: Settings of the pulse sequences used during the ring experiment.

Sequence	**3D-GRE**	**3D-RAVE**
Number of slices	20	20
Matrix size	64x64	128X128
FoV (mm)	160x160	320x320
TE (ms)	10	10
TR (ms)	13	12
Slice thickness (mm)	2.5	2.5
Number of spokes	N/A	256

First, images of the phantom without the ring were recorded. Second, images with the ring (containing phase changes) were recorded. The data of the 3D-RAVE sequence is oversampled by a factor of two on purpose, that is to say, there are twice as many points sampled in order to avoid aliasing artifacts in the region of interest.

3.2 Phantom heating experiment

3.2.1 Phantom fabrication

For the heating experiment, an agar-based phantom is used. Agar has a high melting point ($>$90°C) and is therefore ideal for ablative procedures.[15] The phantom for this study was made with 2% agar. Agar is added to distilled water and heated to 90°C. After the temperature reaches 90°C, the mixture is cooled down to 50°C while stirring. At the temperature of 50°C, the mixture is poured into a measuring cup. For a tissue-mimicking phantom used in ultrasound ablation, the optimal attenuation coefficient should be between 0.3-0.7 dB/cm MHz.[16] The attenuation coefficient of the 2% agar phantom is 0.3 dB/cm MHz.[15]

3.2.2 HIFU system

To facilitate ultrasound ablation, the experimental setup required a HIFU system. This study uses a 1.715 MHz transducer, a signal generator and an amplifier. The agar-based phantom was placed on top of the ultrasound transducer, inside the measuring cup. To avoid cavities forming at the surface of the transducer, a water layer is introduced between the phantom and the transducer. In Figure 3.1 the HIFU transducer is shown.

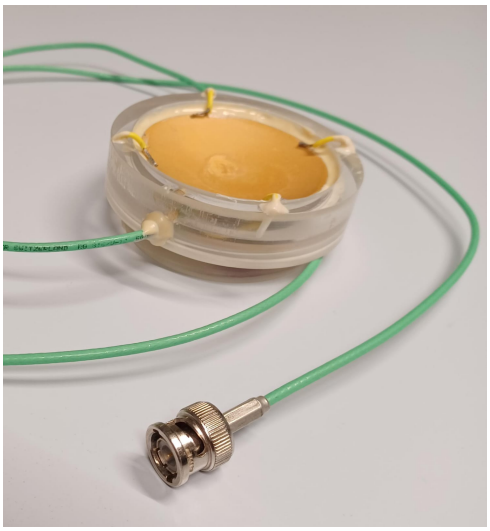

Fig. 3.1: The HIFU transducer. During the ablation procedure, the phantom was placed on top of the transducer with a water layer in between the phantom and the transducer.

To maximize the power delivery to the transducer and minimize reflections, an impedance-matching circuit is employed. This circuit was designed as an LC-circuit.[17] The impedance of the transducer, when coupled with the water layer and laid down into the MRI scanner, was matched to the 50Ω impedance of the amplifier. With a vector network analyzer, the impedance of the transducer at 1.715 MHz was measured and the values for the inductor (L) and capacitor (C) were determined. To achieve the desired matching, a capacitor of 1.87 nF and an inductor of 1.7 μH are required. The designed circuit is shown in Figure 3.2. Instead using a single 1.7 μH inductor, two inductors of 1 μH were connected in series to create an inductance of 2 μH. Additionally, two 3.3 nF capacitors were connected in series to create a capacitance of 1.65 nF instead of the 1.87 nF capacitor.

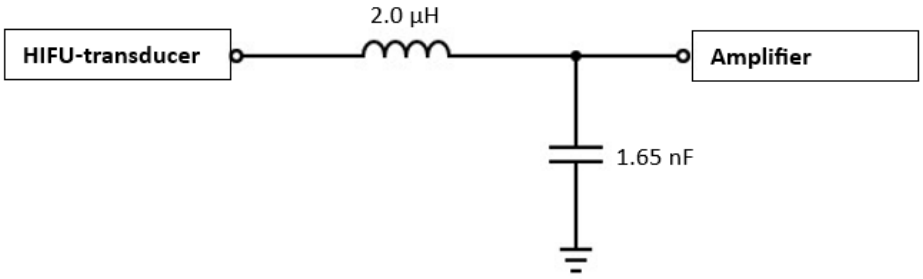

Fig. 3.2: Matching network to match the impedance of the transducer to the 50Ω impedance of the amplifier.

The matching network was tested by measuring the log-magnitude graph as can be seen in Figure 3.3. At the frequency of around 1.7 MHz, the magnitude of the reflection coefficient is -19.91 dB which indicates a weakening of the reflected signal and as a result, around 99% of the power is delivered to the transducer.

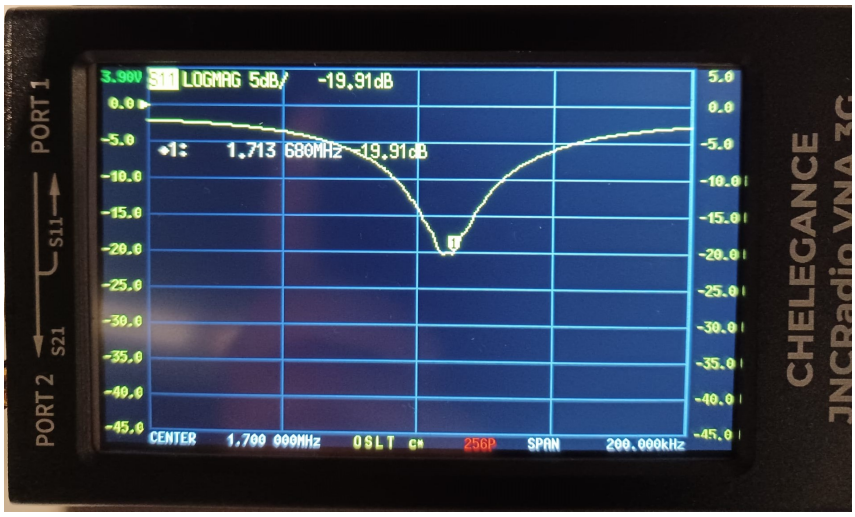

Fig. 3.3: Log-magnitude graph after the matching network was implemented.

The amplifier utilized in this setup provides a voltage gain of 60 dB at 2 MHz. To determine the power delivered to the transducer, Eq. 3.1 is used. The power is driven by a peak-to-peak voltage of 200 mV generated by the signal generator and then amplified to 200 V by the amplifier.

$$P = UI = \frac{U_{RMS}^2}{R} = \frac{(\frac{U_{pp}}{\sqrt{2}})^2}{R} = \frac{20000}{50} = 400W \tag{3.1}$$

In this equation: P represents the power delivered (in Watts). U is the voltage (in Volts). I is the current (in Amperes). U_{RMS} is the root mean square voltage. U_{pp} is the peak-to-peak voltage (200 V in this case). R is the resistance (50Ω, as mentioned earlier).

3.2.3 MRI experiment

For the MR-Thermometry measurements, the experimental setup consisted of a Siemens 1.5T scanner, a 16-channel head coil, a signal generator and an amplifier. The phantom is positioned on top of the HIFU transducer, separated by a layer of water. This entire assembly is placed into the head coil. The transducer is connected to the amplifier through the matching circuit. A fiber optic temperature sensor is inserted into the center of the phantom, close to the transducer's focal point, to make temperature validation possible.

The sequences used during the MR-Thermometry procedure are the 2D-EPI and the 3D-RAVE sequences (performed in P-in-L stacking). In Figure 3.4 the order of the applied sequences is shown. Prior to the ablation procedure, a k-space consisting of 512 spokes per slice is recorded. This data is used to create the baseline image in the k-space hybrid model.

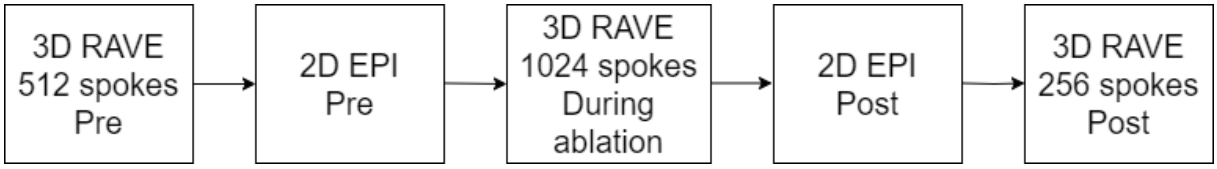

Fig. 3.4: Order of the MRI sequences.

The protocol for both sequences can be seen in Table 3.2. The 3D-RAVE sequence again uses oversampling to avoid aliasing artifacts. The number of spokes differs between the different RAVE acquisitions. The 1024 spokes per slice recorded during the ablation procedure

will be used for dynamic temperature reconstruction. The ablation procedure is performed for approximately three minutes.

Table 3.2: Settings of the pulse sequences used during the phantom heating experiment.

Sequence	**2D-EPI**	**3D-RAVE**
Number of slices	1	16
Matrix size	128X128	128X128
FoV (mm)	320x320	320x320
TE (ms)	10	10
TR (ms)	30	12
Slice thickness (mm)	10	2.5

3.3 Temperature map reconstruction

Temperature maps were reconstructed with MATLAB R2022a according to the k-space hybrid model developed by Gaur et al. As a result of the cartesian sampling in k_z direction, this direction can be transformed to image domain by an inverse discrete Fourier transform as illustrated in Figure 3.5. Now, from each slice, the temperature maps are reconstructed separately.

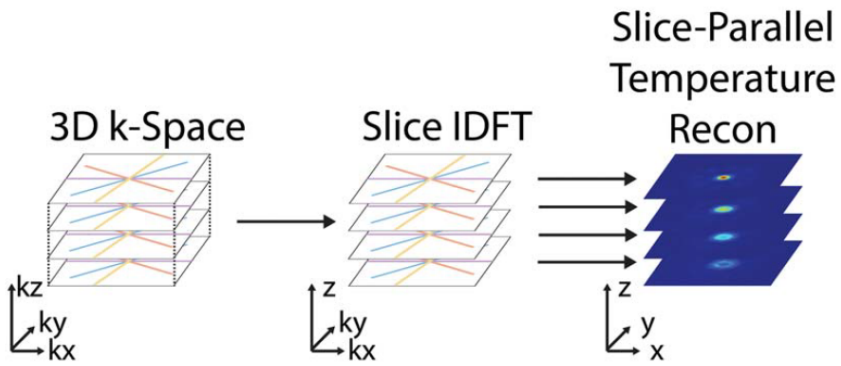

Fig. 3.5: Temperature reconstruction method. First, an image domain in the z direction is created by an inverse discrete Fourier transform. Afterwards, from each k-space slice a temperature map is formed.[7]

The k-space hybrid algorithm uses a baseline image, recorded prior to heating. This baseline image was constructed through a conjugate gradient (CG) reconstruction algorithm, which uses the non-uniform DFT $\boldsymbol{G}$-matrix from Eq. (2.8) to make radial reconstruction possible. Also, sampling density compensation is applied within the baseline image reconstruction. This density compensation is necessary because, in radial trajectories, the center of k-space is sampled more densely compared to the outer region of k-space. As a result, the reconstructed image lacks high frequencies, leading to reduced image sharpness. With a ramp filter, the k-space samples are weighted such that the samples at the outer region of k-space contribute more to the image than the samples in the center region.[18] The reconstructed baseline image is passed to the k-space hybrid algorithm.

In Figure 3.6 the structure of the temperature map processing is shown. The k-space hybrid method requires the raw k-space data acquired during heating, this data may be undersampled. The regularization parameters determine the polynomial order of the $\boldsymbol{Ac}$ term the l_1 penalty weight (λ), to control the sparsity of $\boldsymbol{\theta}$ in Eq. (2.6) and a roughness penalty weight (β) to smooth the temperature map. Third, the coordinates of the sample points are required as input and are

used to form the G-matrix. The density compensation function is the same as for the baseline image. The initial theta matrix consists of the initial temperature phase shift before the ablation procedure. In most cases, this is a zeros matrix with the size of the final temperature map because it is assumed there is no temperature phase shift prior to the ablation procedure. The k-space hybrid algorithm gives the updated temperature phase-shift matrix as output. By multiplying this matrix with $\frac{1}{\gamma \alpha B_0 TE}$ from Eq. (2.4), the temperature matrix is formed and from this, the temperature maps are constructed.

A dynamic reconstruction of temperature maps is made by using different spokes for each frame. For instance, in a sequence where 1024 spokes are acquired, each frame can use 64 spokes. Consequently, in the initial frame, the initial 64 spokes are utilized to generate the temperature map, in the second frame, spokes 65 through 128 are employed, and so forth.

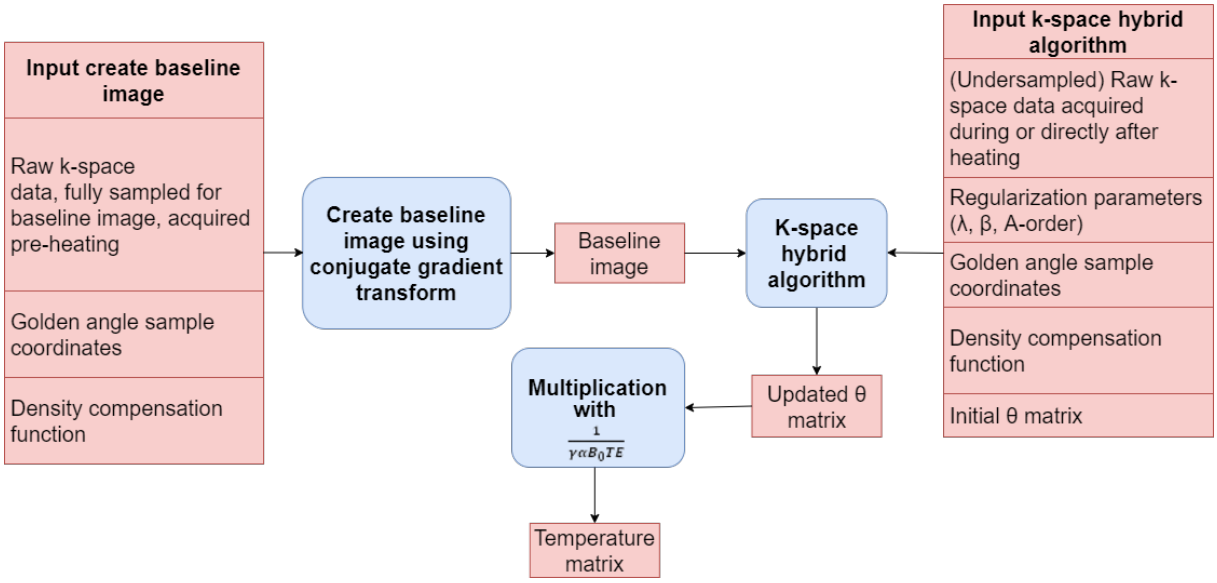

Fig. 3.6: Flow diagram of the temperature map processing. In- and output variables are shown in red, and procedures are shown in blue.

Besides the k-space hybrid reconstruction, a temperature map reconstruction based on the total phase change between two images is performed. Those two images are reconstructed according to the CG reconstruction algorithm. To determine the total phase change between two images Eq. (3.2) is used. In this equation, $M_{i,j}$ and $M_{0,j}$ are the complex images of the j^{th} coil which needs to be compared.[19] $M_{0,j}$ is in this case the baseline image and $M_{i,j}$ is the image recorded after heating.

$$\Delta\phi = arg\left(\sum_{j=1}^{N}(M_{i,j} \cdot M_{0,j}^{*})\right) \tag{3.2}$$

Because the total phase change consists of temperature change and the Ac term from Eq. (2.5), the Ac matrix, determined with the k-space hybrid model, needs to be incorporated into Eq. (3.2). This equation can be rewritten to Eq. (3.3). Again with Eq. (2.4) the temperature difference is determined.

$$\Delta\phi = arg\left(\sum_{j=1}^{N}(M_{i,j} \cdot (M_{0,j} \cdot e^{i\{\boldsymbol{Ac}\}_j})^{*})\right) \tag{3.3}$$

Next to the 3D temperature map reconstructions, temperature maps of the 2D-EPI data were

reconstructed via the k-space hybrid method. In essence, this works the same as for the 3D reconstruction. Except, the baseline image is reconstructed using a 2D FFT and instead of the sample coordinates as input, a sample mask is given as input. This mask is a logic matrix with the size of the k-space, which includes the pixels that need to be used in the k-space hybrid method.

3.4 Temperature validation

The temperature maps of the 3D-RAVE data reconstructed with the k-space hybrid method are validated by comparing these maps with CG-reconstructed temperature maps. The temperature accuracy of the 3D-RAVE data will be assessed based on the deviation of the temperature compared to the CG maps. In particular, the voxel with the maximum temperature is an important parameter.[7] The voxel where the maximum temperature is reached within the k-space hybrid reconstruction will also be used in the determination of the acceleration factor. From now on, this particular voxel is called the target voxel.

Next to the CG-reconstructions as reference data, a fiber optic temperature sensor is placed in the phantom. This sensor measures the temperature change near the focus during the ablation procedure. Based on a high-resolution image, the voxel location of the sensor is determined. The temperature accuracy at this voxel location is assessed by comparing the temperature measured by the sensor and the temperature measured by MR-thermometry.

3.5 Acceleration factor

To determine the maximum acceleration factor, temperature maps with different numbers of spokes are created. The spokes are selected from the 3D-RAVE data recorded during ablation. For each number of spokes, the central spokes are employed. In other words, out of the 1024 spokes recorded during ablation, when reconstructing with, for instance, 64 spokes, the central 64 spokes of each slice are selected. The acceleration factor is given by $\frac{N_{spokes\ fully\ sampled}}{N_{spokes\ undersampled}}$. In this study, each slice sampled with at least 256 spokes is defined as fully sampled.

Also, temperature error maps are reconstructed using the first 256 spokes of the 3D-RAVE pre-dataset for the baseline image. The raw data is formed out of the second 256 spokes of this 3D-RAVE pre-dataset. For each different number of spokes, the first spokes of this data set were selected. So for the error map op 64 spokes, the baseline image is formed out of the first 256 spokes and the raw data is then formed from spoke 257 to 320 from the 3D-RAVE pre-dataset. Between the recording of the baseline image and the raw data, there was no heating. The method to reconstruct temperature error maps is described in detail in Ref. [6]. Shortly, the k-space hybrid algorithm is run twice. In the first run, only a step to update the c-term is executed, while θ is fixed at zero. In the second run, the θ-update step is executed, while the c value found from the first run is used.

4 RESULTS

4.1 Ring experiment

In Figure 4.1 the phase images obtained with the 3D-GRE sequence are presented. Figure 4.1a displays the phase image of the phantom without the ring (the baseline image). Figure 4.1b is the phase image of the phantom with the ring where a phase change is induced. Figure 4.1c represents the total phase shift between the images with and without the ring. Only negative phase shift is considered because this corresponds to temperature increase. Figure 4.1d shows the phase shift map resulting from temperature change of the tenth slice from the ring experiment obtained with the 3D-RAVE sequence. This map is reconstructed using the k-space hybrid method. A zeroth-order polynomial is employed as Ac term and the regularization parameters are set to default ($\lambda = 10^{-6}$ and $\beta = -1$). Upon comparing the phase map from Figure 4.1d with the phase images in Figure 4.1c it can be seen that the total phase shift in Figure 4.1c corresponds to the phase shift in Figure 4.1d.

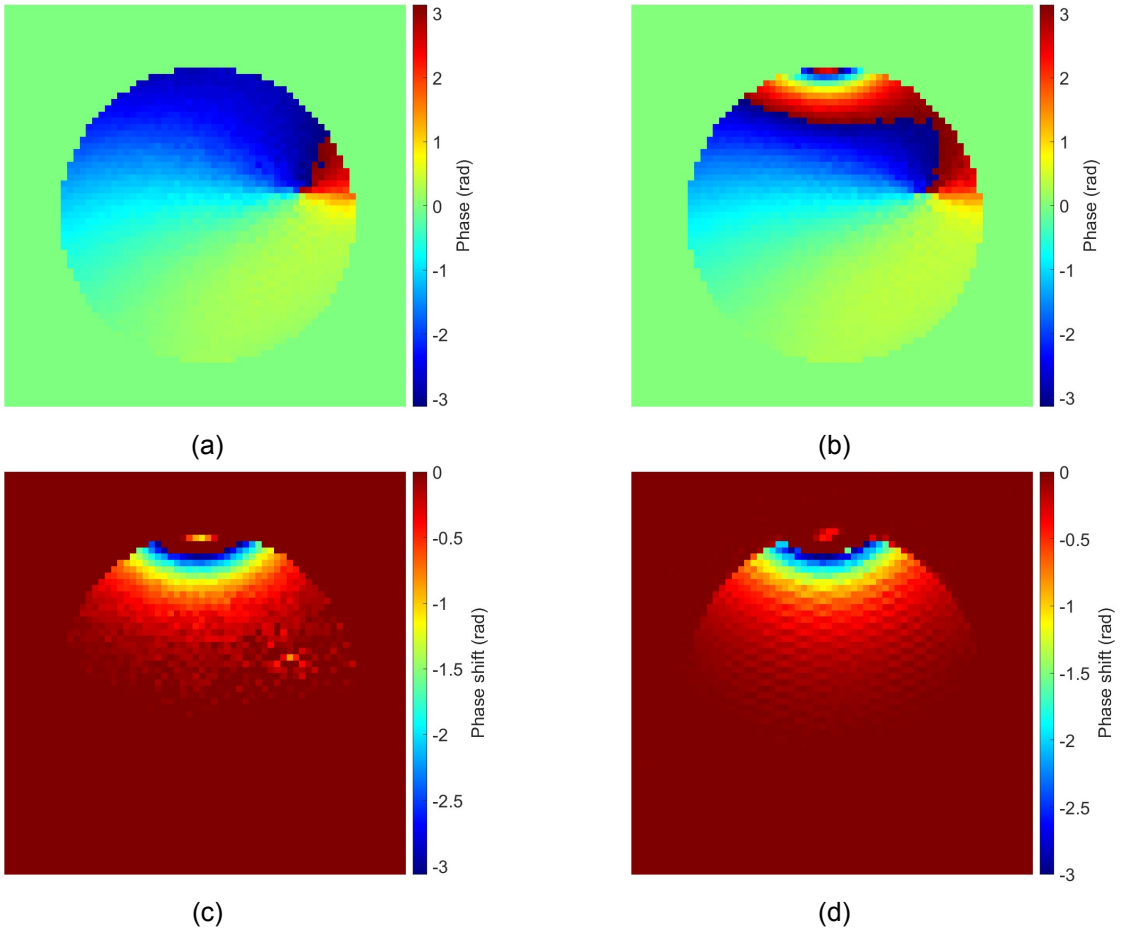

Fig. 4.1: Phase images of the phantom a,b and c are acquired with 3D-GRE sequence, d is acquired with the 3D-RAVE sequence. The tenth slice is displayed. (a) Phantom without the metal ring. (b) Phantom with the metal ring. (c) Total phase shift between the images with and without ring. Only negative shift is taken into account. (d) Phase shift map reconstructed with the k-space hybrid method.

4.2 Phantom heating experiment

This section contains the results of the phantom heating experiment. The temperature maps of the 3D-RAVE data, including a dynamic temperature map and error maps of different acceleration factors are shown. Next to that, the temperature map of the 2D-EPI data is provided. A magnitude image XY-plane of the phantom, with the HIFU transducer and water positioned beneath it, is shown in Figure 4.2. For the 3D data, slice 8 is chosen for reconstructing the 2D images. This slice is the central slice and also contains the target voxel.

The regularization parameters are set to $\lambda = 10^{-4}$ and $\beta = -1$ (no roughness penalty) and a first-order polynomial for A, for all the reconstructions within this section. This decision is based on the reconstructed figures in Appendix B. Upon varying λ it is observed that for $\lambda = 10^{-3}$, the temperature map is completely zero. Comparing the images where $\lambda = 10^{-4}$ and $\lambda = 10^{-5}$, the maximum temperature for $\lambda = 10^{-5}$ is slightly higher. The heating of the water is more visible when $\lambda = 10^{-5}$. When varying the order of A, the zeroth order yields a slightly higher maximum temperature than the first order and the second order gives a slightly lower maximum temperature compared to the first order. Incorporating the β-parameter leads to a smoother image, but it also corresponds to a lower maximum temperature.

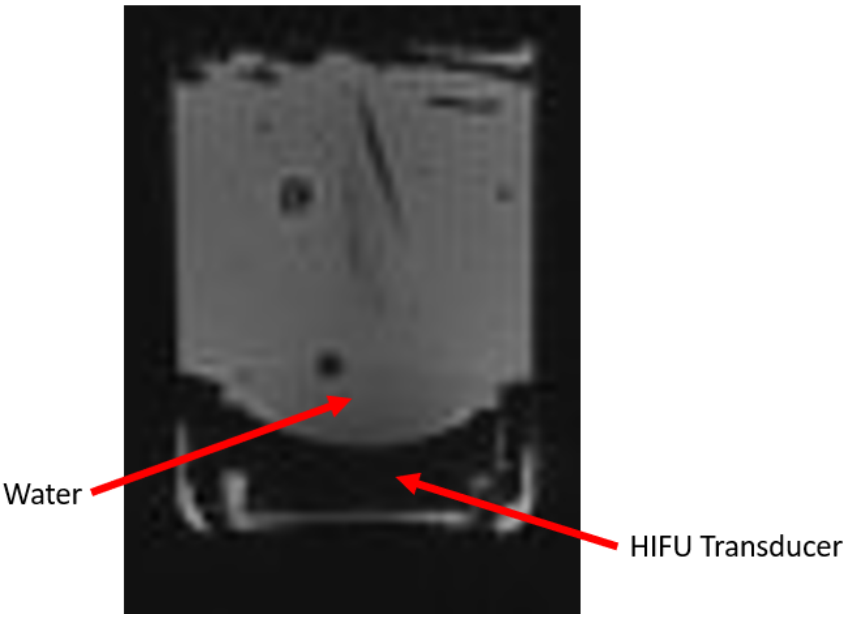

Fig. 4.2: Magnitude image of the XY plane of the phantom with water and the HIFU transducer beneath it.

4.2.1 Fiber optic temperature sensor

Figure 4.3 illustrates the graph of the temperature change of the phantom, recorded during and after ablation, measured with the fiber optic sensor. The ablation procedure lasted for approximately 190 seconds. The total temperature change during the ablation procedure is approximately 14 °C. The temperature graph is not completely linear during ablation. After ablation, an immediate cooling down is visible.

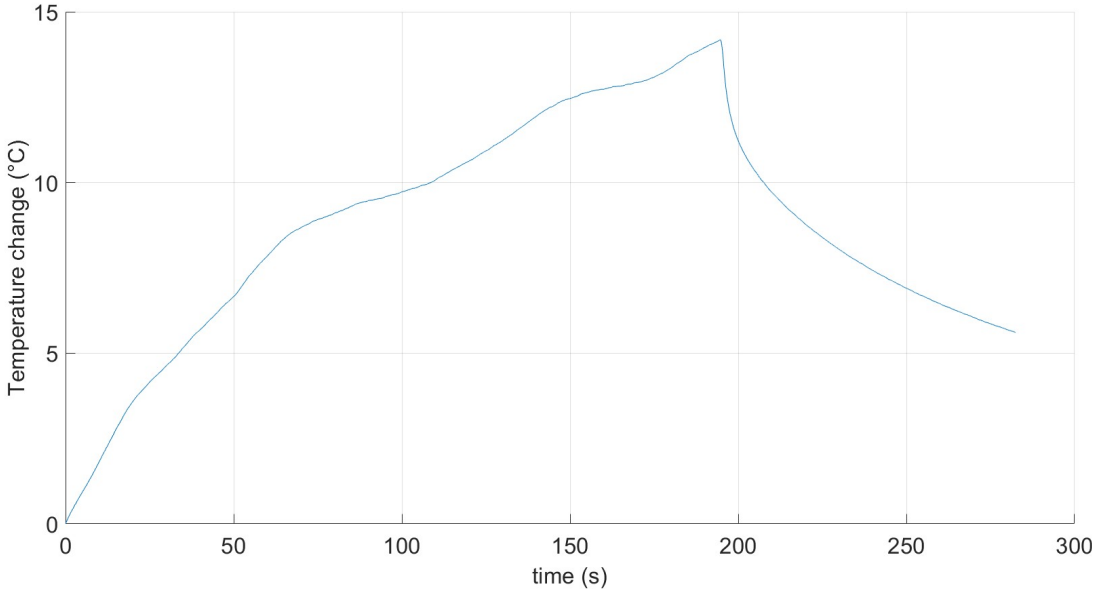

Fig. 4.3: Temperature graph measured during and after ablation near the focal point with a fiber optic temperature sensor.

4.2.2 2D-reconstruction

In Figure 4.4 the temperature maps of the 2D-EPI data are shown. Figure 4.4a is reconstructed with the k-space hybrid algorithm and Figure 4.4b is reconstructed with an ordinary Fourier transform. The latter figure is masked to prevent distraction from the phase changes in the air, outside the phantom. This mask can be found in Figure D.1b in Appendix D. The mask does not cover the entire outer region, therefore, below the water, a small line of phase change outside the phantom is visible.

In Figure 4.4a, the temperature of the target voxel is 12 °C. In Figure 4.4b this temperature is 12.2 °C. In both figures, the target voxel is not the hottest voxel of the focus. The real maximum temperatures are 12.4 °C for Figure 4.4a and 12.6 °C for Figure 4.4b. This voxel is located right below the target voxel.

The temperature in the voxel where the fiber optic sensor is located is 9.7 °C for the k-space hybrid reconstruction and 9.9 °C for the Fourier reconstruction. Notably, this EPI sequence was recorded approximately 5 seconds after the ablation procedure. As depicted in Figure 4.3, the temperature measured by the sensor at this specific timestamp approximates 11 °C.

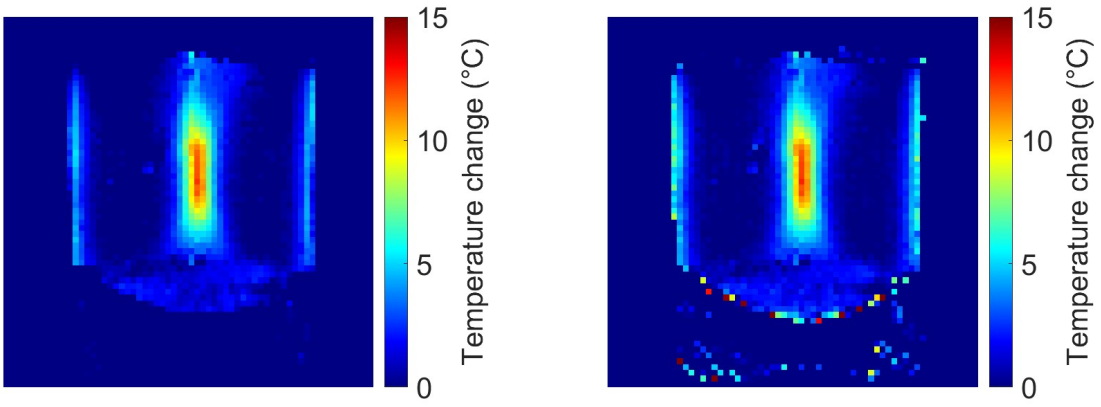

(a) (b)

Fig. 4.4: Temperature maps of the 2D-EPI data (a) K-space hybrid reconstruction. (b) Fourier transform reconstruction.

4.2.3 3D-reconstruction

4.2.3.1 K-space hybrid reconstructions

Figure 4.6 illustrates two planes of temperature maps of the 3D-RAVE sequence reconstructed with the k-space hybrid method. The two planes intersect each other at the target voxel and their orientations can be found in Figure 4.5 The maps are made with the last 256 spokes of the 3D-RAVE pre-data used for the baseline image and the 3D-RAVE post-data as the raw k-space data, capturing the temperature change. Within the phantom, the maximum temperature reached is 10.7 °C. It is evident from the maps that not only the focus of the transducer is heated, but also the sides of the phantom contain a small temperature change. The maximum temperature change at the sides of the phantom is approximately 3 °C.

The 3D-RAVE post image was captured approximately 36 seconds after the ablation procedure. The temperature at the voxel where the sensor is located is 8.4 °C. The temperature measured by the sensor at this timestamp is approximately 8 °C as can be seen in Figure 4.3.

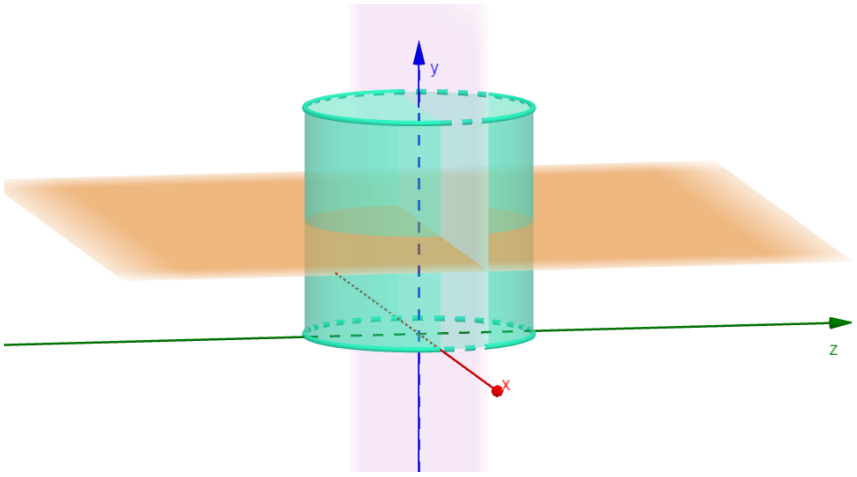

Fig. 4.5: Orientation of the planes used for displaying temperature maps. The planes intersect each other at the target voxel.

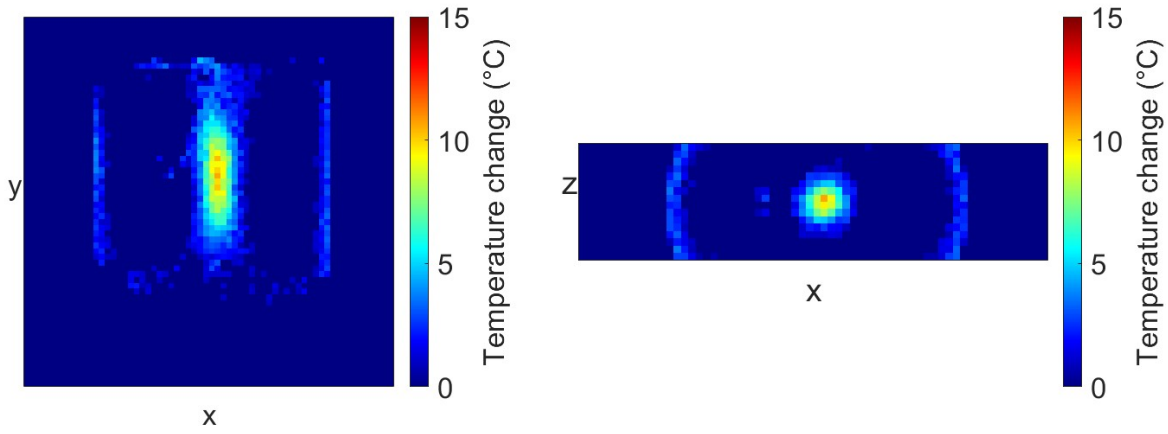

(a) XY-plane (b) XZ-plane

Fig. 4.6: Temperature maps from different planes of the 3D-RAVE sequence reconstructed with the k-space hybrid method

4.2.3.2 Conjugate Gradient reconstruction

In Figure 4.7 the temperature maps of the 3D-RAVE sequence, reconstructed according to the CG reconstruction algorithm, are presented. Those images are again masked with the mask in Figure D.1b. The two planes look quite similar to the images in Figure 4.6. Within the CG-reconstruction method, no regularization penalty is applied. Therefore, the heating of the water is more visible. On the left side of the focus, in Figure 4.7a, a small spot, containing temperature change is visible. This spot is likely the air bubble on the left side of the fiber, as also observable in Figure 4.2. The target voxel temperature is 12.8 °C. This voxel is actually the voxel with the maximum temperature within this map. The temperature at the voxel of the sensor location is 9.4 °C.

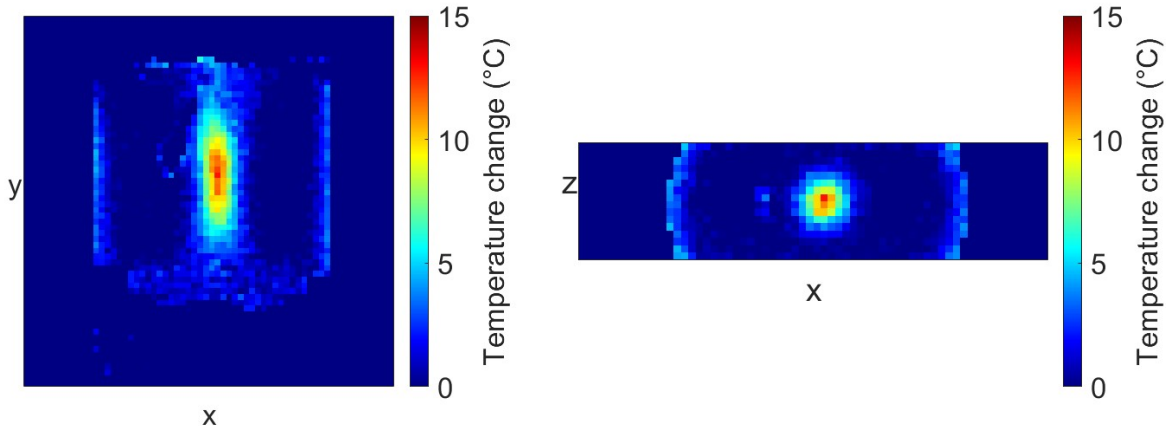

(a) XY-plane (b) XZ-plane

Fig. 4.7: Temperature maps from different planes of the 3D-RAVE sequence reconstructed with the CG reconstruction algorithm.

4.2.3.3 Temperature difference

Figure 4.8 represents the temperature difference between the maps reconstructed using the k-space hybrid method and the CG-reconstruction algorithm. Throughout almost the entire phantom, the temperature change obtained with the k-space hybrid method appeared to be lower than the temperature obtained with the CG-reconstruction algorithm. Near the focus, the temperature difference is approximately 2 °C, which is slightly higher than in the rest of the phantom. There, the difference is approximately 1 °C. In the water, the difference is also slightly higher than in the rest of the phantom, this is due to the fact that heating of water is more visible in the CG reconstructed images.

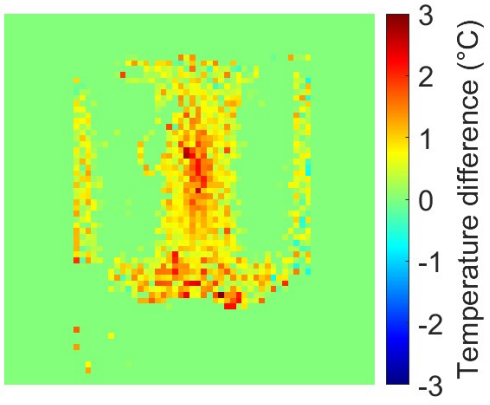

Fig. 4.8: Temperature difference between the k-space hybrid reconstruction and the CG-reconstruction.

4.2.4 Acceleration factor

Figure 4.9 contains images of the XY-plane of the 3D-RAVE sequence, each reconstructed with different numbers of spokes. These reconstructions were made with the k-space hybrid method, where the last 256 spokes of the 3D-RAVE pre-data are used for the baseline image and the 3D-RAVE HIFU data as the raw k-space data.

The images reconstructed with 128 spokes or more resemble each other. From the 64-spokes reconstruction, down to the 8 spokes reconstruction, more temperature noise is visible. For all numbers of spokes, the focus remains discernible, although, for 8 spokes it becomes more difficult to distinguish the focus from the surroundings.

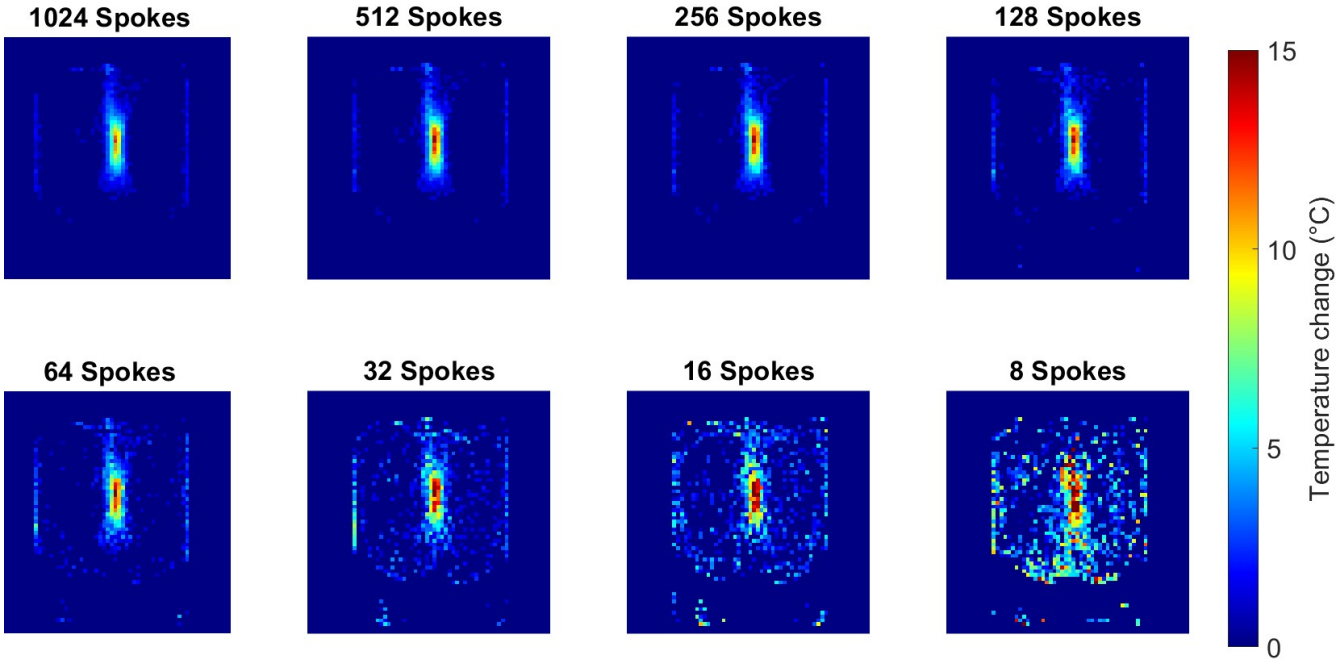

Fig. 4.9: Temperature maps reconstructed with the k-space hybrid method using different numbers of spokes.

Table 4.1 presents the values for the temperature of the target voxel. The voxel with the actual highest temperature does not always coincide with the target voxel. For instance, in the 8 spokes reconstruction, voxels outside the focus exhibit a higher temperature than the target voxel. Overall, a trend of increasing temperatures with fewer spokes is observed, with the exception of the temperature for 64 spokes being higher than that for 32 spokes.

Table 4.1: Temperature of the target voxel at different numbers of spokes within a k-space hybrid reconstruction.

Number of spokes	**1024**	**512**	**256**	**128**	**64**	**32**	**16**	**8**
Target voxel temperature (°C)	12.7	14.5	14.5	14.6	16.4	15.5	16.4	18.6

Figure 4.10 displays the temperature error maps of the k-space hybrid reconstructions at different numbers of spokes. These images are reconstructed using the first 256 spokes of the 3D-RAVE pre-data as baseline image and the last 256 spokes of the 3D-RAVE pre-data as raw k-space data. Importantly, no ablation is performed between these two datasets. According to Ref.[13], 200 spokes is a full sampled k-space. For 256 spokes there is no error visible, as expected for a fully sampled image. For 128 spokes, a minor temperature error across the entire phantom becomes noticeable. As the number of spokes decreases further, larger error values are visible.

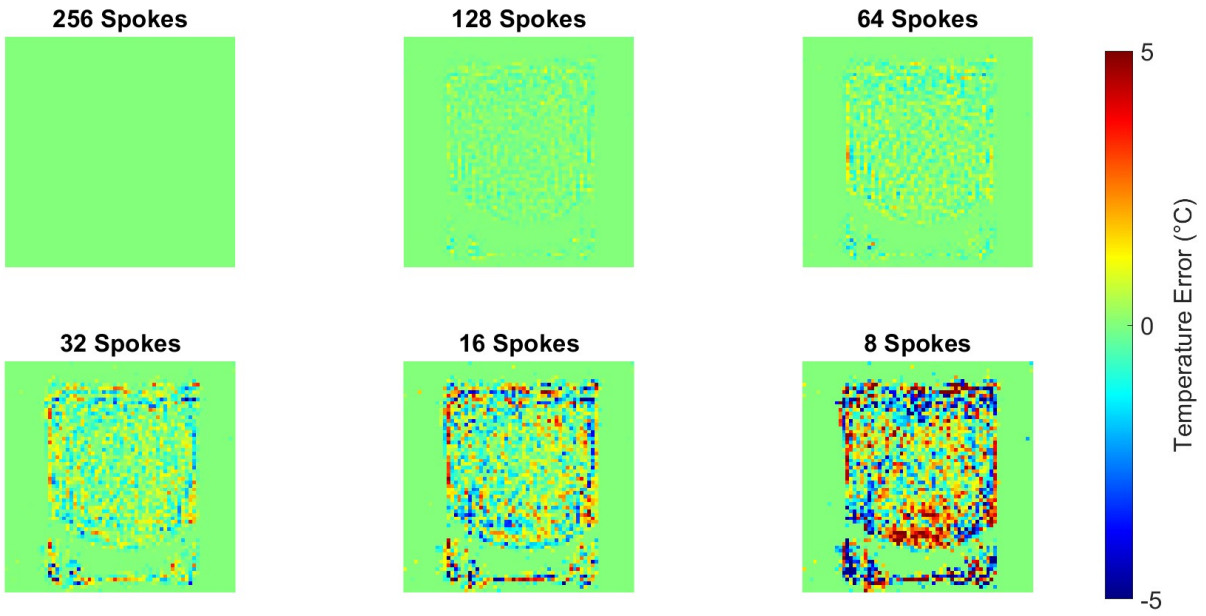

Fig. 4.10: Temperature error maps of the k-space hybrid reconstruction for different numbers of spokes.

Boxplots of the temperature errors are shown in Figure 4.11. They indicate that the interquartile ranges and the overall spread increase with fewer spokes, while the median remains around zero for all boxplots. For 64 spokes the interquartile range runs from -0.3 to 0.3 °C and the adjacent values lie at -1.1 and 1.2 °C. The maximum outlier value is -2.6 °C. For 32 spokes the interquartile range spans from -0.5 to 0.6 °C and the adjacent values lie at -2.2 and 2.3 °C. The maximum outlier value is -5.0 °C.

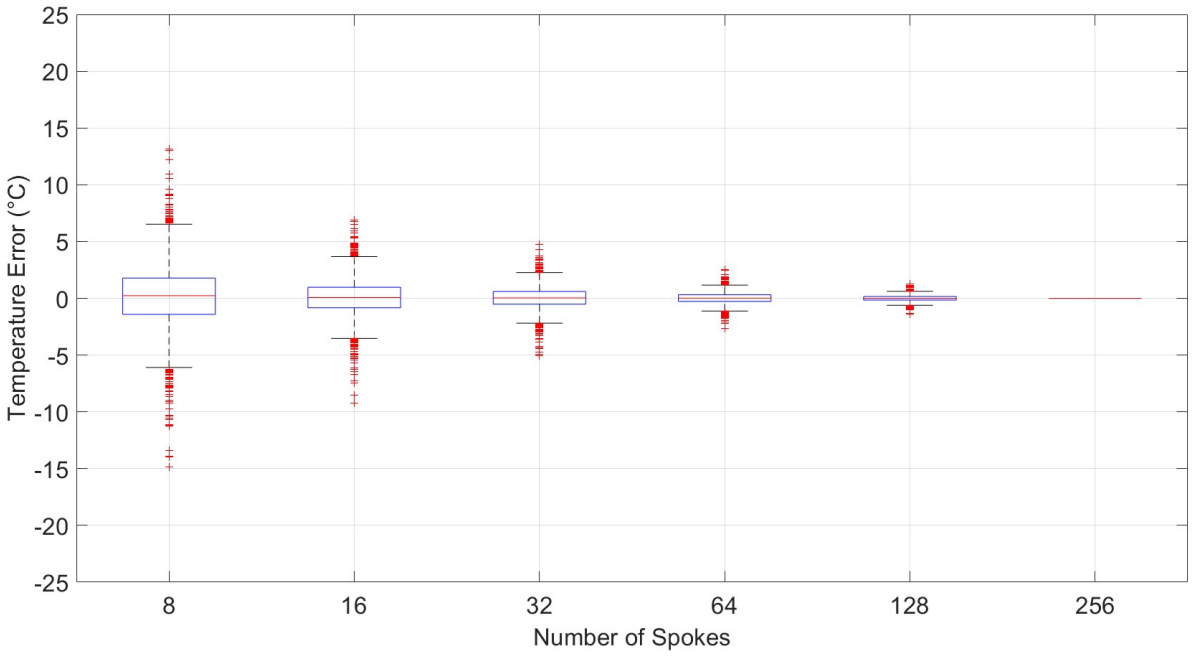

Fig. 4.11: Boxplots of the temperature error of the k-space hybrid reconstruction for different numbers of spokes.

In Figure 4.12 the temperature maps for different numbers of spokes, reconstructed with the CG reconstruction algorithm are shown. It is evident that, similar to the k-space hybrid reconstruc-

tions, the noise increases for fewer spokes. Compared to the k-space hybrid reconstructions, the CG-reconstructions demonstrate a more rapid increase in the amount of noise over the number of spokes. For 16 or 8 spokes, the temperature map appears more blurred, making it more difficult to distinguish the focus from its surroundings. This effect is probably due to the undersampling, where high spatial frequencies are not sampled enough to satisfy the Nyquist criterion.

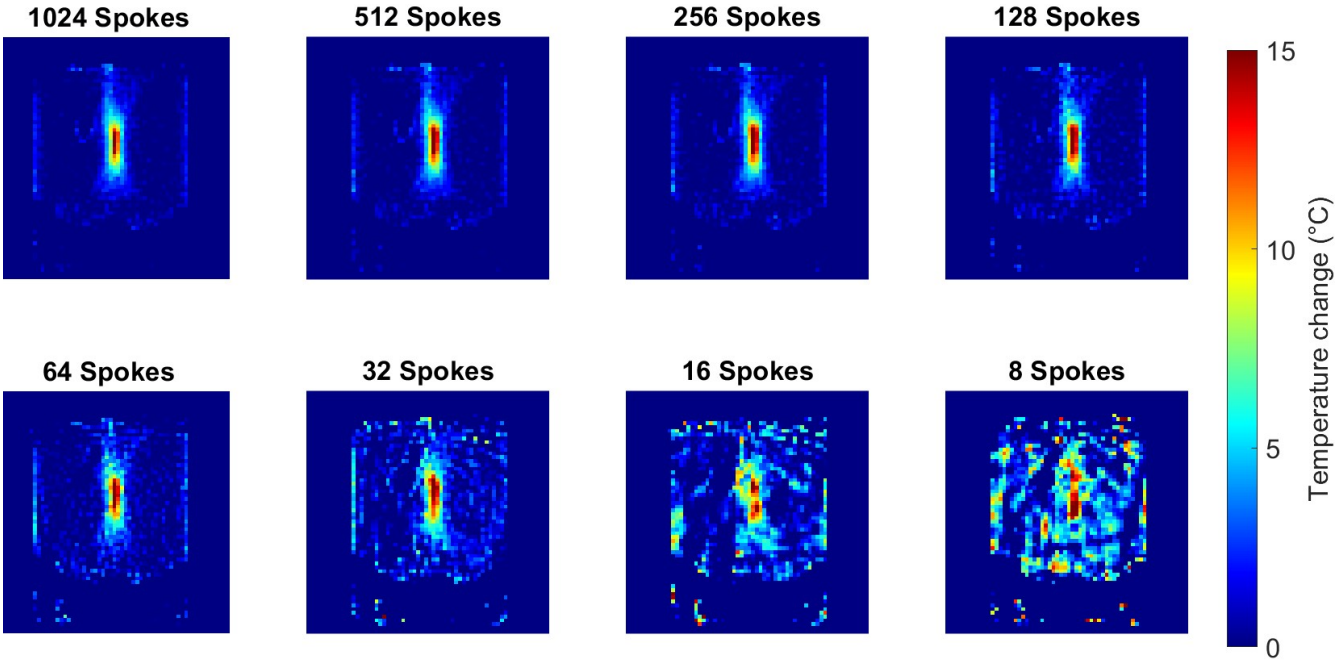

Fig. 4.12: Temperature maps reconstructed with CG reconstruction algorithm with different numbers of spokes.

The temperatures of the target voxel for the CG-reconstruction are provided in Table 4.2. In this case, there is not a clear relationship as observed for the target voxel temperature within the k-space hybrid reconstruction, where an increase of the temperature at fewer voxels was visible.

Table 4.2: Temperature of the target voxel at different numbers of spokes within a CG-reconstruction.

Number of spokes	**1024**	**512**	**256**	**128**	**64**	**32**	**16**	**8**
Target voxel temperature (°C)	17.4	19.2	18.9	19.1	19.8	16.5	11.1	13.4

Figure 4.13 illustrates the temperature error maps for different numbers of spokes, reconstructed with the CG reconstruction algorithm. Like the error maps for the k-space hybrid reconstructions, the temperature error increases for fewer spokes. Surprisingly, even for 256 spokes, expected to represent a fully sampled k-space, a small temperature error is visible.

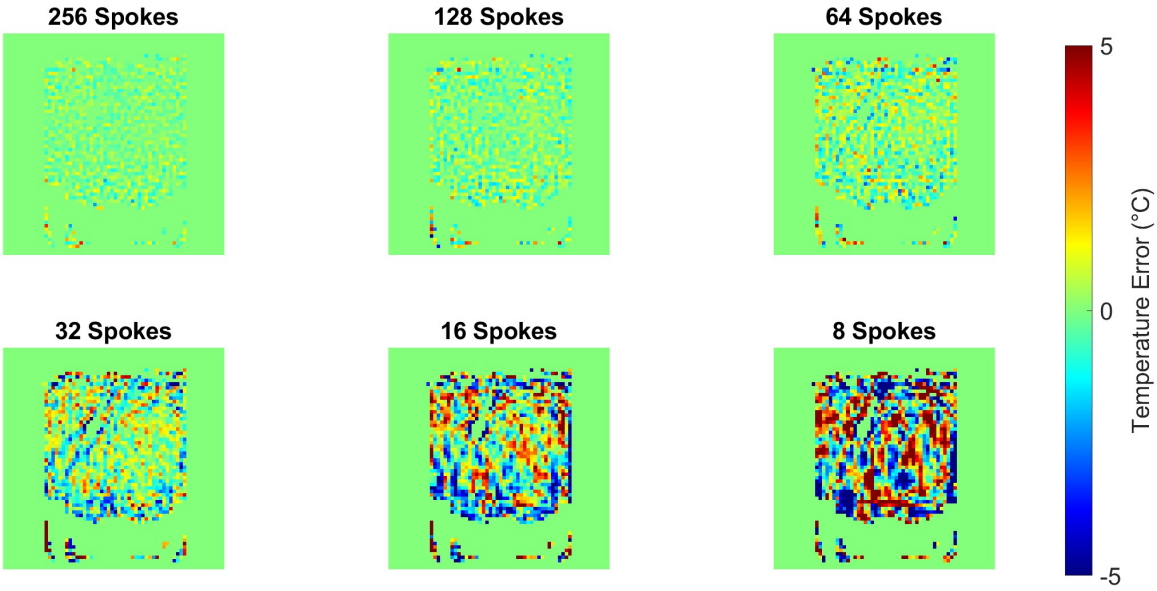

Fig. 4.13: Temperature error maps of the CG-reconstruction for different numbers of spokes.

In Figure 4.14 the corresponding boxplots of the CG error maps are shown. Again, the interquartile ranges and the overall spread increase with fewer spokes. The median for all numbers of spokes is located close to zero.

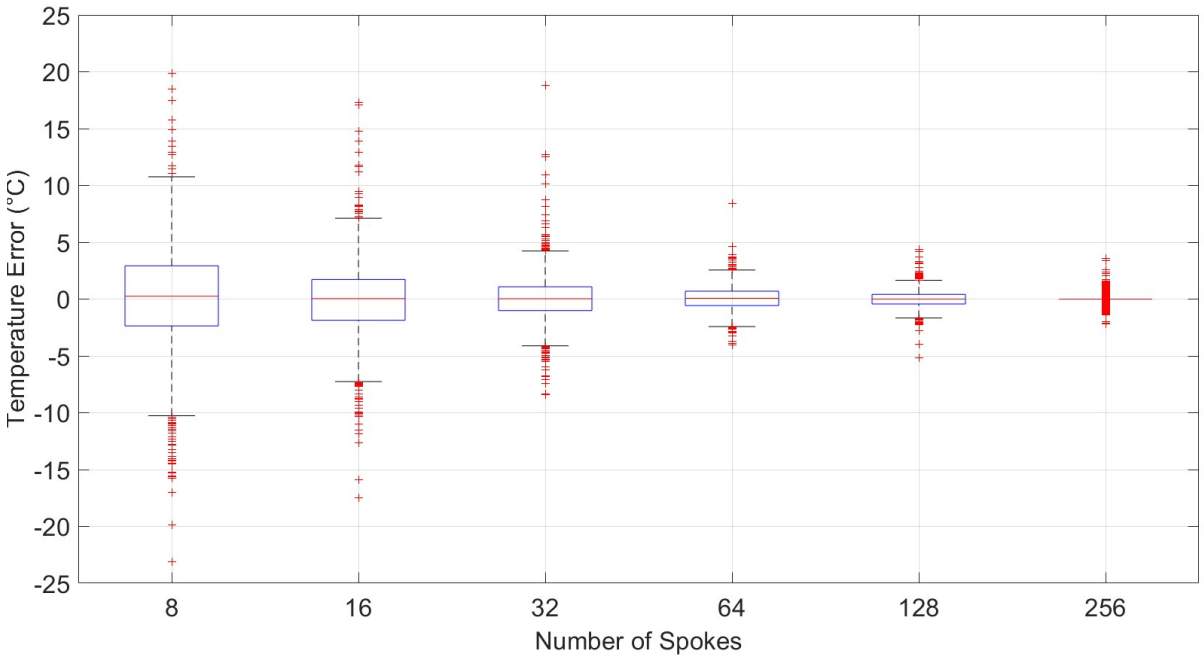

Fig. 4.14: Boxplots of the temperature error of the CG-reconstructions for different numbers of spokes.

4.2.5 Real-time temperature mapping

Figure 4.15 shows a dynamic development of the focus during the ablation procedure. Four frames of a total of 16 frames are presented. The frames are reconstructed with 64 spokes each. The focus gets bigger as more time has passed.

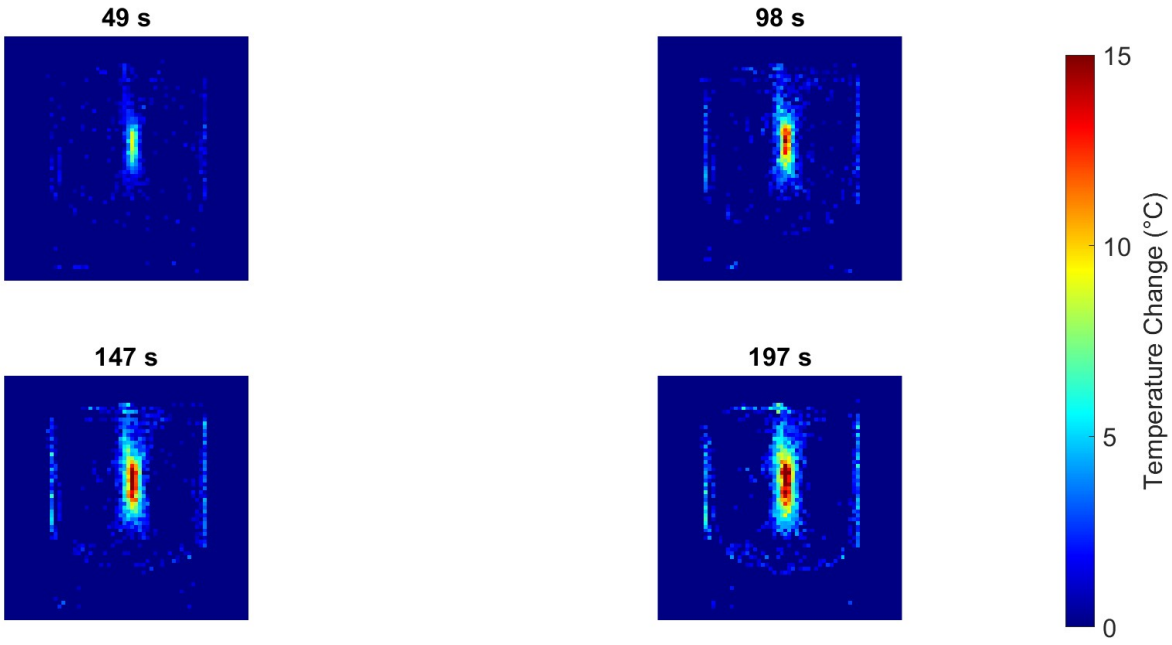

Fig. 4.15: Development of focus during the ablation procedure at different timestamps. Every frame is reconstructed with 64 spokes. From the 16 frames, each fourth frame is shown.

Figure 4.16 illustrates the corresponding temperature graph of the voxel where the sensor is located temperature. As expected, the temperature in the focus increases further in time. Errorbars, based on the adjacent values in Figure 4.11 are added. By comparing this graph to the graph in Figure 4.3, the overall temperature measured with the sensor is higher. In Appendix C the real-time temperature graphs of reconstructions with 32, 128 and 256 spokes are shown.

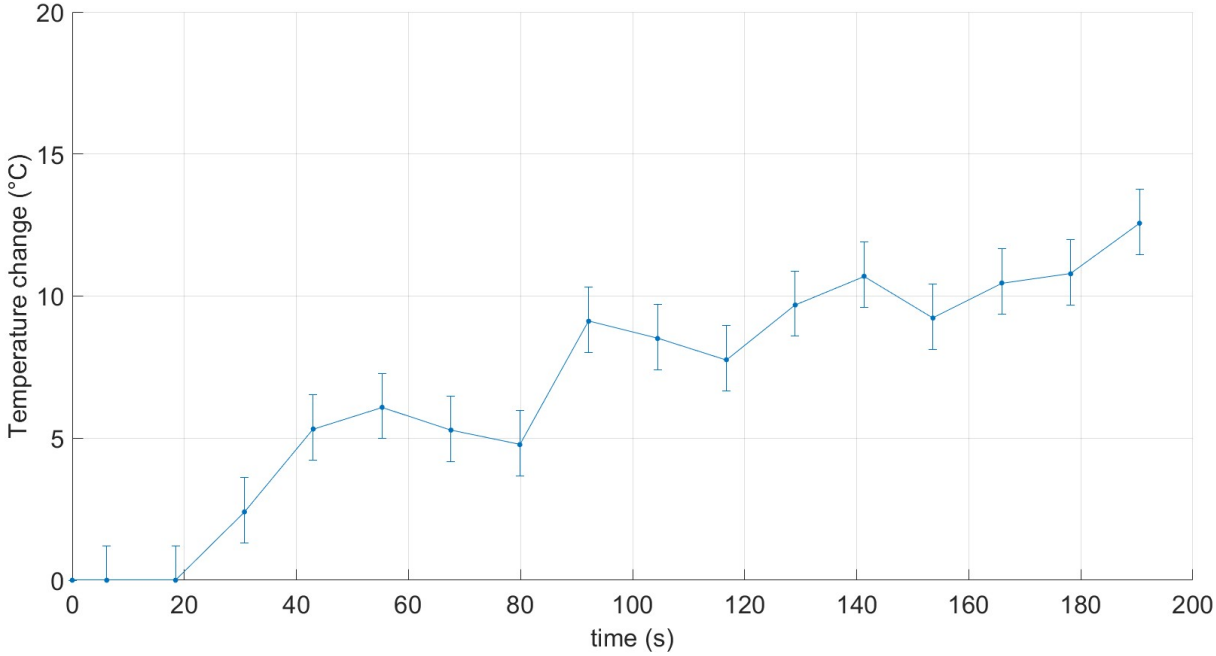

Fig. 4.16: Graph of the temperature against time. Each point (containing an errorbar) corresponds to the different frames, where each frame is reconstructed with 64 spokes. The voxel location is the location of the sensor.

5 DISCUSSION

This study focused on the use of a 3D Stack-Of-Stars Gradient Echo (3D-RAVE) pulse sequence, combined with the k-space hybrid reconstruction method developed by Gaur et al. [6] for monitoring temperature changes during ablation procedures. The great advantage of this Golden Angle sampling is the uniform distribution of k-space samples, independent of the number of spokes. Besides, radial sampling ensures that the center of the k-space is sampled each TR. This center contains most of the image contrast and therefore key information about the peak temperature. The k-space hybrid method facilitates temperature map reconstruction with undersampled k-space data, thereby enabling real-time temperature mapping at a high frame rate.

Two experiments were performed to investigate the use of this sequence for (real-time) temperature mapping. The first experiment, the ring experiment, was used to prepare the k-space hybrid MATLAB script for the actual ablation experiment. With this dataset, phase maps were successfully reconstructed using the k-space hybrid method. From this preparation, it was found that, in order to prevent aliasing artifacts, the 3D-RAVE data should be oversampled. Oversampling, in this case, meant that twice as many points per spoke needed to be sampled. Instead of oversampling, another possibility could be using a mask with the size of the radial FOV. The use of a mask was also investigated and the results can be found in Appendix D. Two different masks were created and applied to the k-space data. It appeared that with the masks, in the case of undersampling, the amount of noise was higher in the images with 128 spokes or less, for the temperature maps reconstructed with the masks compared to the temperature maps reconstructed with oversampling. Also, in the error maps and boxplots, it is visible that the spread of the error is larger for the mask reconstructions. Even for 256 spokes a small error is visible in both mask reconstructions. Not only does the oversampled reconstruction differ from the mask reconstruction, but also between the two mask reconstructions a difference in peak temperatures and errors appeared.

The second experiment involved a HIFU setup to perform a thermal ablation procedure in a phantom. Temperature maps were created using the k-space hybrid method and a conventional reconstruction method in both 2D and 3D. When comparing the temperature maps created with the k-space hybrid method with the (fully sampled) conventional reconstruction method, in general, the temperature in the maps of the k-space hybrid reconstructions was lower than the temperatures in the conventional reconstructed maps. For the 2D maps, this difference was smaller than for the 3D maps. In the 3D case, the temperature difference between the two reconstruction methods was approximately 2 $^{\circ}$C for the hottest voxel and 1 $^{\circ}$C for the voxel where the sensor was located. Near the focus, the temperature difference was bigger than further away from the focus.

When comparing the temperature measured with MR-thermometry with the temperature measured with the sensor, it became evident that the temperature derived from the 3D maps was closer to the sensor temperature than that derived from the 2D maps. This finding suggests that 3D temperature mapping may offer a higher level of accuracy and reliability compared to 2D temperature maps. Between the two 3D reconstructions, the temperature of the sensor location for the CG-reconstruction was higher than the k-space hybrid temperature. The k-space hybrid temperature was closer to the sensor temperature. This implies that the k-space hybrid reconstruction is more accurate than the CG-reconstruction.

The voxel location of the sensor was determined with a high-resolution image. Based on the approximate voxel location in this image, the location of the sensor in the 3D-RAVE maps was determined. Because this determination is not 100% accurate it could be possible that the sensor location was at a different voxel than the voxel currently used. If this is the case, the difference between the sensor temperature and the MRI-acquired temperature might be much larger or smaller. When zooming in into a smaller region of the k-space hybrid temperature map, as has been done in Figure 5.1, it can be seen that between each column of voxels, a strong spatial gradient in the temperature distribution exists. So if the exact location of the sensor was in a different column, the temperature measured in this voxel would be different from the current measured temperature.

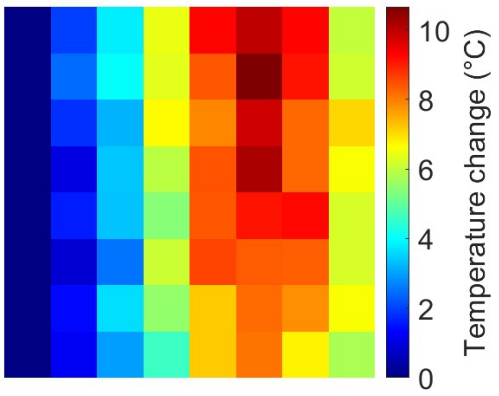

Fig. 5.1: Zoomed in region of the k-space hybrid temperature map. Large temperature differences between the columns of voxels are visible.

For clinical use of this sequence, it is important that the smoothness of these temperature maps improve. One way to achieve a smoother temperature map is by acquiring the data at a higher resolution. In this way transitions between neighbouring voxels become less abrupt. Nevertheless, a high-resolution image means a longer scan time and thus a lower frame rate. Particularly for real-time temperature mapping, this is a problem.

Furthermore, modifying the regularization parameters was found to influence the smoothness of the temperature map. As can be seen in Appendix B the β parameter influences the smoothness of the temperature map, so by changing this value, the transitions between the voxels become less abrupt. Changing this value also has an influence on the temperature, the higher the β value, the lower the temperature. Not only does the β parameter have an influence on the temperature, but also the λ parameter and the order of A have an influence on the temperature. This was the case in both the 2D and 3D reconstructions. Especially in the regions where a higher temperature is reached, the regularization parameters have an influence. This may explain why the temperature difference between CG and k-space hybrid is larger in the focus. Those regularization parameters are application specific and further research is needed to make sure the right regularization parameters are used.

In order to increase the temperature precision for PRF measurements, the signal-to-noise ratio (SNR) should be maximized. Temperature uncertainty depends on the SNR by Eq.(5.1)

$$\delta T = \frac{dT}{d\phi} \cdot \frac{\sqrt{2}}{SNR} = \frac{1}{2\pi\gamma B_0 \alpha [TE]} \cdot \frac{\sqrt{2}}{SNR} \tag{5.1}$$

SNR depends on the B_0 field by $SNR \propto B_0$, therefore, if instead of a 1.5T scanner a 3T scanner was used, the SNR was increased with a factor of 2 and thus temperature uncertainty is reduced by a factor $\sqrt{2}$.[20] A second parameter that has an effect on the SNR is the receiver bandwidth. The lower this bandwidth, the higher the SNR. Nevertheless, a lower bandwidth could result in a shift of the hotspot due to off-resonance effects.[21] It could be interesting to investigate what the optimal receiver bandwidth would be for MR-thermometry with the 3D-RAVE sequence.

Another thing that stood out and could have had an influence on the measured temperature was a change in the magnitude image of the 3D-RAVE pre and the 3D-RAVE post. In Figure 5.2 the magnitude image of the 3D-RAVE pre and the 3D-RAVE post are shown. On the 3D-RAVE post image, a dark spot is visible at the location of the heating.

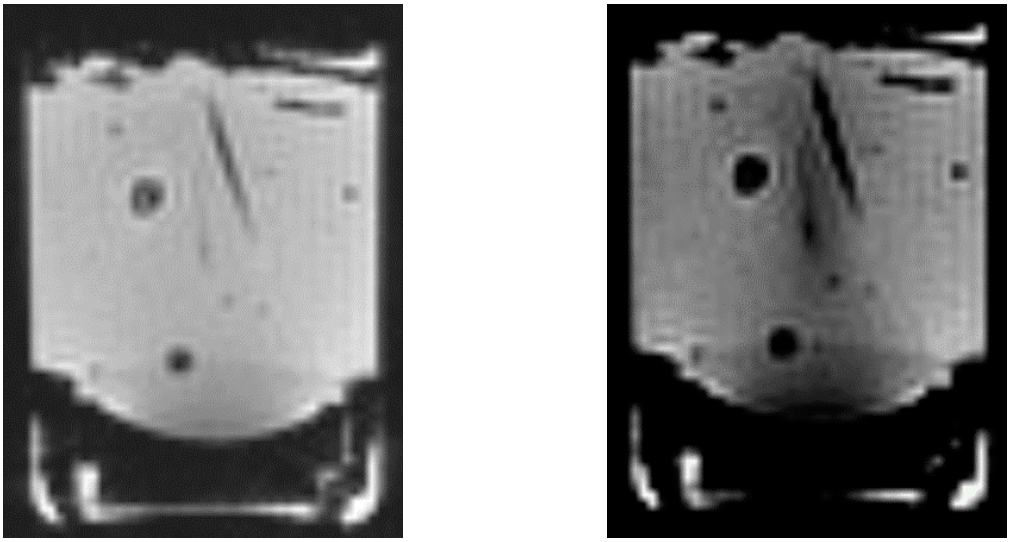

(a) Pre ablation image (b) Post ablation image

Fig. 5.2: Magnitude images of the 3D-RAVE. A decrease of magnitude is visible at the location of heating.

According to Ref.[3], not only phase changes with temperature but also proton density, T1 or T2 can change. Those changes cause a difference in the magnitude image. To incorporate this temperature-related magnitude change into the k-space hybrid model, θ should become a complex matrix. To determine the temperature shift due to phase change, only the real part of theta should be used in Eq 2.4. It should be investigated if this is incorporated into the algorithm.

The second part of this study focused on determining the minimum number of spokes that need to be sampled in order to get a reliable temperature map. Based on the temperature maps created with the different numbers of spokes it can be seen that for more than 128 spokes, little noise is visible. When the number of spokes further decreases, more noise comes into the temperature maps due to undersampling. Up to 16 spokes the region of the focus was clearly visible. The error maps showed an increase in error for fewer spokes. Within the k-space hybrid method for 64 spokes, the adjacent values showed a positive error of 1.2 °C and a negative error of -1.1 °C. The number of outliers for each boxplot is quite big. This means that certain voxels will have a larger error than the error between the adjacent values. Based on these results, it can be concluded that for 64 spokes or more quite accurate temperature maps can be created. 64 spokes correspond to an acceleration factor of 4. Because different processes due to ablation do not happen at precise temperatures but at temperature regions, a small error in the measured temperature is acceptable. It does not matter if a certain region is heated up to 60 °C or to 65 °C for the outcome of the treatment. For the efficiency of the treatment not

only the peak temperature reached during ablation is an important parameter, but also the size of the region that is heated is important. Based on the results, this is possible with as few as 16 spokes when the k-space hybrid method is used. Nevertheless, For 16 spokes, the error range between the adjacent values is -3.7 to 3.5 °C.

In the error maps in Figure 4.10 there is no clear relationship between the error value and the location. This is probably due to the uniformity of the phantom. In Ref.[6] error maps of the head were made for different numbers of spokes and it seemed that most of the errors occurred at specific areas of the head. For in vivo use, it might be interesting to investigate if different tissue types have an influence on the error.

Comparing the real-time temperature graph in Figure 4.16 to the graph measured with the sensor, the course of the sensor graph is much smoother than the course of the graph made with MR-thermometry due to the number of sampling points. In the MR-thermometry graph, certain outliers are visible, probably due to temperature errors. Overall, the temperature of the sensor graph is higher than the MR-thermometry graph. This is the case for all numbers of spokes, even for a fully sampled image with 256 spokes, where the temperature of the sensor voxel is approximately 2 °C lower than the actual temperature measured by the sensor. This result is contradictory to the results of the temperature maps based on the pre and post datasets, where the difference between the sensor and the sensor voxel was only 0.4 °C. It should be investigated what causes this difference between the sensor and sensor voxel during dynamic imaging. If the temperature map is formed with more spokes, the graphs become smoother, as is visible in Appendix C. For 256 spokes it can be seen that the last measured point is earlier in time than for fewer spokes. Also, for 256 spokes it takes longer to record all the spokes. Within this time interval, the temperature continues to increase and the temperature measured at the time of the first spoke is smaller than the temperature when the last spoke is recorded. Probably, to create the temperature map, the algorithm searches for an average temperature between the first and the last spoke. For dynamic temperature mapping, the rate of heating during the ablation procedure should be adjusted to the frame rate of the pulse sequence.

Undersampling was also performed with the CG-reconstruction method. Comparing these to the k-space hybrid undersampled temperature maps, the error within the undersampled CG maps was larger. In the boxplots in Figure 4.14 it is noticeable that the spread of the error is larger for the CG-reconstructed maps than for the k-space hybrid reconstructed maps. Also, for 16 spokes the region of the focus is less clearly visible than for the k-space hybrid reconstructions. This proves that the k-space hybrid method indeed performs better for undersampled images.

To speed things up a little bit, fewer slices can be used if the k_z sampling direction is perpendicular to the propagation direction of the ultrasound beam. This is because unexpected heating is often found in the near- and far fields of the ultrasound beam. In the direction perpendicular to the beam, no heating outside the focus will occur so only the focus needs to be captured, which is for example also possible with 8 slices instead of 16 slices in this study.

If the number of slices cannot be reduced, because a large volume coverage is required, an interesting option might be the k_z accelerated variable-density stack-of-stars pulse sequence (VD-stack-of-stars).[22] This sequence makes use of the same golden angle sampling in the k_x-k_y plane but in the z-direction, only the center part is fully sampled. The outer part is not sampled uniformly. Most of the temperature information is located in the center of k-space, therefore undersampling the outer region of the k_z-direction would not extremely affect the measured temperature. In Figure 5.3 the principle of this sequence is shown. A disadvantage of this

sampling scheme is the more complicated reconstruction because in z-direction a fast Fourier transform is not possible in this case. Nevertheless, it would be interesting to investigate if this sequence works for MR-thermometry to increase the frame rate, the slice resolution or the volume coverage.

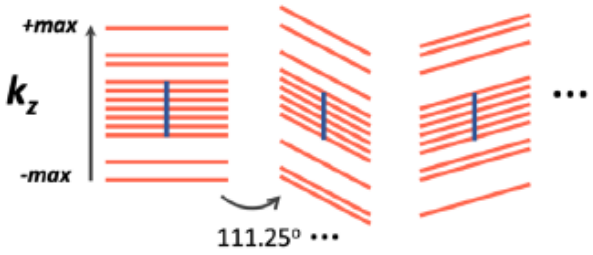

Fig. 5.3: Principle of the VD-stack-of-stars sequence. The k_z direction is not sampled uniformly. This sequence makes it possible to increase volume coverage, frame rate or slice resolution. [14]

A second interesting sequence is a different variable density Golden Angle Stack-of-Stars sampling but in this case, the k_z dimension is sampled uniformly and the variable density is applied in the different number of spokes per slice as can be seen in Figure 5.4.[23] Due to the uniformity in k_z-direction, a fast Fourier transform is possible in this case.

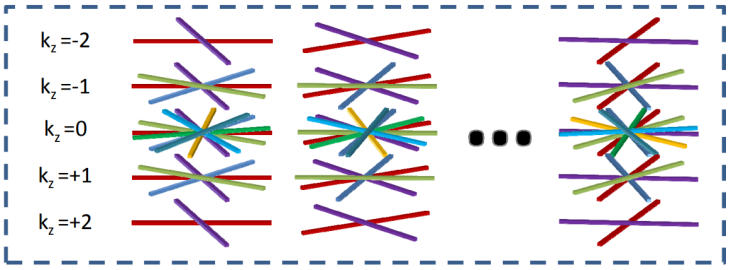

Fig. 5.4: Principle of the variable density Golden Angle Stack-of-Stars sampling sequence. The number of spokes differs per slice. This sequence makes it possible to increase the frame rate.[23]

In previous years, several other pulse sequences for volumetric MR-imaging have been investigated. One of those sequences is the 3D Stack-of-Stars Echo-Planar pulse sequence.[7] The principle of the sequence is almost the same as the 3D-RAVE sequence except that the gradient echo planes used in the 3D-RAVE sequence are replaced by EPI planes which are rotated 111.25°after each TR. The big advantage of using an EPI sequence is the higher frame rate compared to a GRE sequence. For the 3D-RAVE sequence, it takes one TR to record each spoke, while for the EPI sequence, a whole plane is recorded in only one TR. The 3D-RAVE sequence used with 64 spokes, 16 slices and a TR of 12 ms can be executed at a frame rate of $64 \cdot 16 \cdot 12 * 10^{-3} = 12.3$ seconds per frame. The 3D SoS EPI sequence used in Ref.[7] uses a TR of 47 ms to record 43 slices. For 64 spokes, this corresponds to a frame rate of $64 \cdot \frac{16}{43} \cdot 47 * 10^{-3} = 1.1$ seconds per frame for 16 slices. So, the EPI sequence is much faster than the 3D-RAVE sequence.

Lastly, it is worth noting that the reconstruction time for the k-space hybrid reconstruction was very long. Specifically, for the 3D reconstruction where 16 slices had to be reconstructed, it took about 30 minutes. Using a GPU might speed up this reconstruction a bit, but for applications where the temperature maps need to be reconstructed in real-time and not afterwards, like in this study, the k-space hybrid algorithm is not fast enough.

6 CONCLUSION

The use 3D Stack-of-Stars Gradient Echo sequence in combination with the k-space hybrid method was investigated for use during an ablation procedure. Based on these results, the 3D Stack-of-Stars Gradient Echo sequence, when fully sampled, can measure temperature change during an ablation procedure. The accuracy for the temperature map based on the pre and post datasets and reconstructed according to the k-space hybrid method was approximately 0.5 °C. For the dynamic measurements, this accuracy was a bit lower. A difference of approximately 2 °C between the sensor and the sensor voxel was found for fully sampled images. There is room for improvement in the temperature accuracy, particularly through the optimization of regularization parameters and the improvement of the SNR.

Also, the results indicate that tracking of the heating region is possible with as few as 16 spokes. With 16 spokes, an error of approximately $\pm$3.5 °C should be taken into account. For most HIFU ablation therapies an error of 3.5 °C might be too large because this can lead to insufficient ablation or unwanted damage to surrounding tissues. An error of $\pm$1 °C is acceptable, this is reached with 64 spokes or more. Using 16 spokes corresponds to an acceleration factor of 16 and a frame rate of 3 seconds per frame whereas 64 spokes corresponds to an acceleration factor of 4 and a frame rate of 12 seconds per frame. Using more spokes increases the accuracy but decreases the frame rate. In clinical use, a careful consideration should be made regarding the balance between the required accuracy for the treatment and the desired frame rate.

REFERENCES

[1] C. Brace. Thermal tumor ablation in clinical use. *IEEE Pulse*, 2(5):28–38, 2011.

[2] E. M. Knavel and C. L. Brace. Tumor ablation: common modalities and general practices. *Tech Vasc Interv Radiol*, 16(4):192–200, 2013.

[3] V. Rieke and K. Butts Pauly. Mr thermometry. *J Magn Reson Imaging*, 27(2):376–90, 2008.

[4] W. A. Grissom, V. Rieke, A. B. Holbrook, Y. Medan, M. Lustig, J. Santos, M. V. McConnell, and K. B. Pauly. Hybrid referenceless and multibaseline subtraction mr thermometry for monitoring thermal therapies in moving organs. *Med Phys*, 37(9):5014–26, 2010.

[5] Mingming Zhu, Ziqi Sun, and Chin K. Ng. Image-guided thermal ablation with mr-based thermometry. *Quantitative Imaging in Medicine and Surgery*, 7(3):356–368, 2017.

[6] P. Gaur and W. A. Grissom. Accelerated mri thermometry by direct estimation of temperature from undersampled k-space data. *Magn Reson Med*, 73(5):1914–25, 2015.

[7] Sumeeth V. Jonathan and William A. Grissom. Volumetric mri thermometry using a three-dimensional stack-of-stars echo-planar imaging pulse sequence. *Magnetic Resonance in Medicine*, 79(4):2003–2013, 2018.

[8] B. T. Svedin, A. Payne, Jr. Bolster, B. D., and D. L. Parker. Multiecho pseudo-golden angle stack of stars thermometry with high spatial and temporal resolution using k-space weighted image contrast. *Magn Reson Med*, 79(3):1407–1419, 2018.

[9] Y. F. Zhou. High intensity focused ultrasound in clinical tumor ablation. *World J Clin Oncol*, 2(1):8–27, 2011.

[10] Thomas Kahn and Harald Busse. *Interventional Magnetic Resonance Imaging*. Medical Radiology. Springer Berlin, Heidelberg, 1 edition, 2012. Hardcover ISBN: 978-3-642-20705-1, Published: 26 August 2012.

[11] P. J. Hore. *Nuclear Magnetic Resonance*. Oxford University Press, August 1995.

[12] Alexa Semonche, Evan Luther, Katherine Berry, Ashish Shah, Daniel Eichberg, Long Di, Michael Kader, and Michael E. Ivan. Mr-guided laser interstitial thermal therapy for treatment of brain tumors. In Alba Scerrati and Pasquale De Bonis, editors, *Neurosurgical Procedures*, chapter 6. IntechOpen, Rijeka, 2019.

[13] Kai Tobias Block, Martin Uecker, and Jens Frahm. Undersampled radial mri with multiple coils. iterative image reconstruction using a total variation constraint. *Magnetic Resonance in Medicine*, 57(6):1086–1098, 2007.

[14] L. Feng. Golden-angle radial mri: Basics, advances, and applications. *J Magn Reson Imaging*, 56(1):45–62, 2022.

[15] T. Drakos, A. Antoniou, N. Evripidou, T. Alecou, M. Giannakou, G. Menikou, G. Constantinides, and C. Damianou. Ultrasonic attenuation of an agar, silicon dioxide, and evaporated milk gel phantom. *J Med Ultrasound*, 29(4):239–249, 2021.

[16] Ari Partanen, Charles Mougenot, and Teuvo Vaara. Feasibility of Agar□Silica Phantoms in Quality Assurance of MRgHIFU. *AIP Conference Proceedings*, 1113(1):296–300, 04 2009.

[17] M. Garcia-Rodriguez, J. Garcia-Alvarez, Y. Yañez, M. J. Garcia-Hernandez, J. Salazar, A. Turo, and J. A. Chavez. Low cost matching network for ultrasonic transducers. *Physics Procedia*, 3(1):1025–1031, 2010.

[18] J. G. Pipe and P. Menon. Sampling density compensation in mri: rationale and an iterative numerical solution. *Magn Reson Med*, 41(1):179–86, 1999.

[19] Z. Zhang, T. Michaelis, and J. Frahm. Towards mri temperature mapping in real time-the proton resonance frequency method with undersampled radial mri and nonlinear inverse reconstruction. *Quant Imaging Med Surg*, 7(2):251–258, 2017.

[20] René M. Botnar, Paul Steiner, Benjamin Dubno, Peter Erhart, Gustav K. von Schulthess, and Jörg F. Debatin. Temperature quantification using the proton frequency shift technique: In vitro and in vivo validation in an open 0.5 tesla interventional mr scanner during rf ablation. *Journal of Magnetic Resonance Imaging*, 13(3):437–444, 2001.

[21] Samuel Fielden, Li Zhao, Wilson Miller, Xue Feng, Max Wintermark, Kim Butts Pauly, and Craig Meyer. Spiral-based 3d mr thermometry. *Journal of Therapeutic Ultrasound*, 3(1):1–3, 2015.

[22] Zhitao Li, Chenchan Huang, Angela Tong, Hersh Chandarana, and Li Feng. Kz-accelerated variable-density stack-of-stars mri. *Magnetic Resonance Imaging*, 97:56–67, 2023.

[23] Z. Li, B.P. Berman, M.I. Altbach, J.P. Galons, D.R. Martin, B. Dong, P. Sharma, N. Raghunand, and A. Bilgin. Highly accelerated 3d dynamic imaging with variable density golden angle stack-of-stars sampling. In *Proceedings of the 21st Annual Meeting & Exhibition of the International Society for Magnetic Resonance in Medicine (ISMRM)*, April 20-26 2013.

A NUMBER OF SPOKES DERIVATION

In order to meet the requirements for the Nyquist criterion, in a cartesian grid the following statement yields.

$$\Delta k \leq \frac{1}{FOV} \tag{A.1}$$

For a radial trajectory, this criterion can be rewritten to

$$k_{max}\alpha \leq \frac{1}{FOV} \tag{A.2}$$

Here, $k_{max}\alpha$ is the arc length between two neighbouring spokes and is our new Δk.

From Nyquist we know that

$$N_{samples} = 2k_{max} \cdot FOV \tag{A.3}$$

For the number of spokes, within a full spoke radial trajectory it yields that

$$N_{spokes} = \frac{\pi}{\alpha} \tag{A.4}$$

If we substitute equation A.2 into A.4 we obtain

$$N_{spokes} = \pi k_{max} FOV \tag{A.5}$$

Using equation A.3 we get

$$N_{spokes} = \frac{\pi}{2} N_{samples} \tag{A.6}$$

B REGULARIZATION PARAMETERS

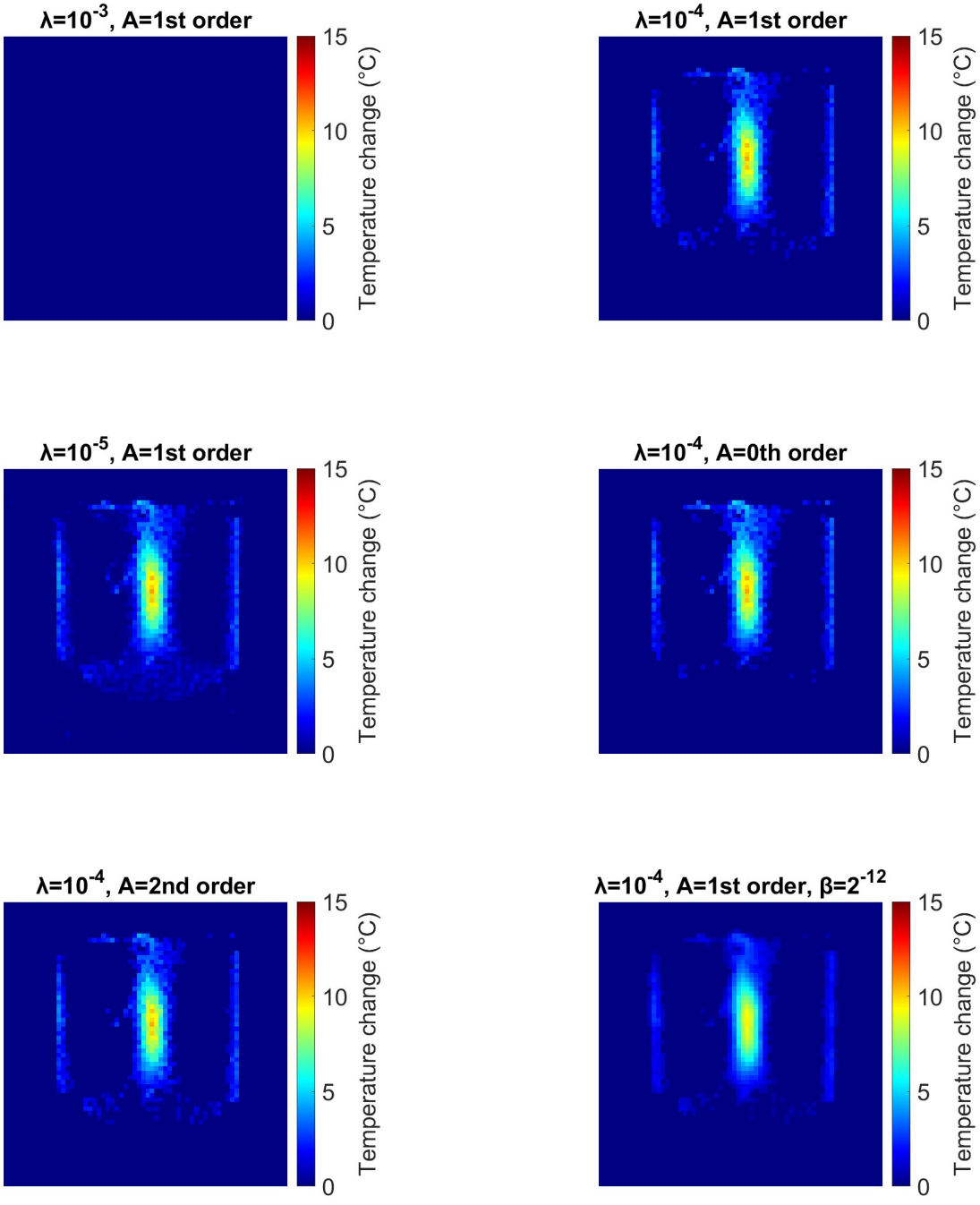

Fig. B.1: Temperature maps with different regularization parameters.

C REAL-TIME TEMPERATURE GRAPHS

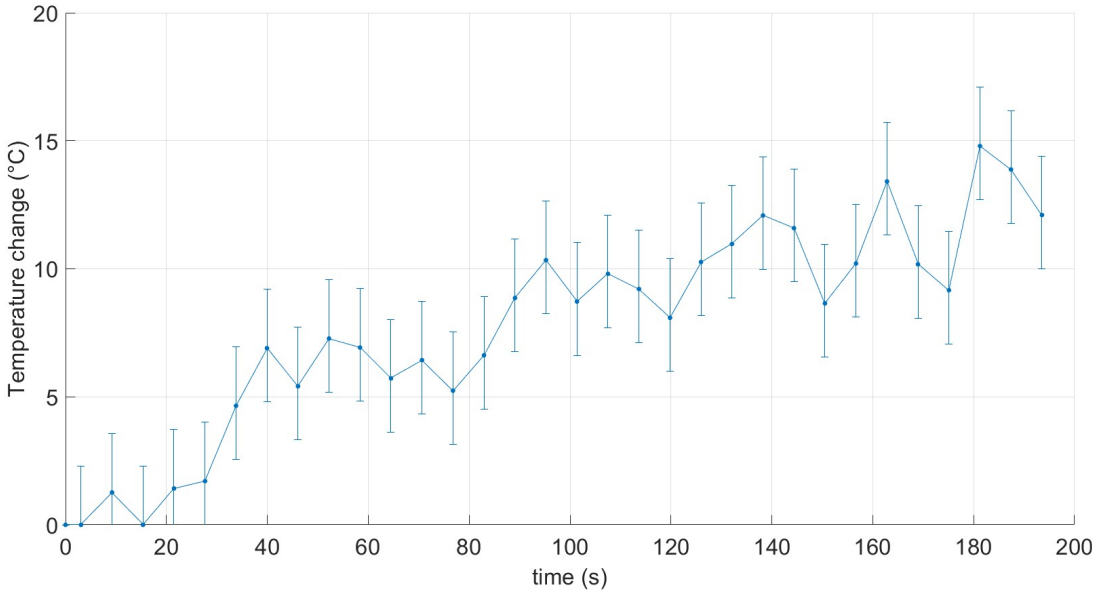

Fig. C.1: Real-time temperature graph reconstructed with 32 spokes for each frame.

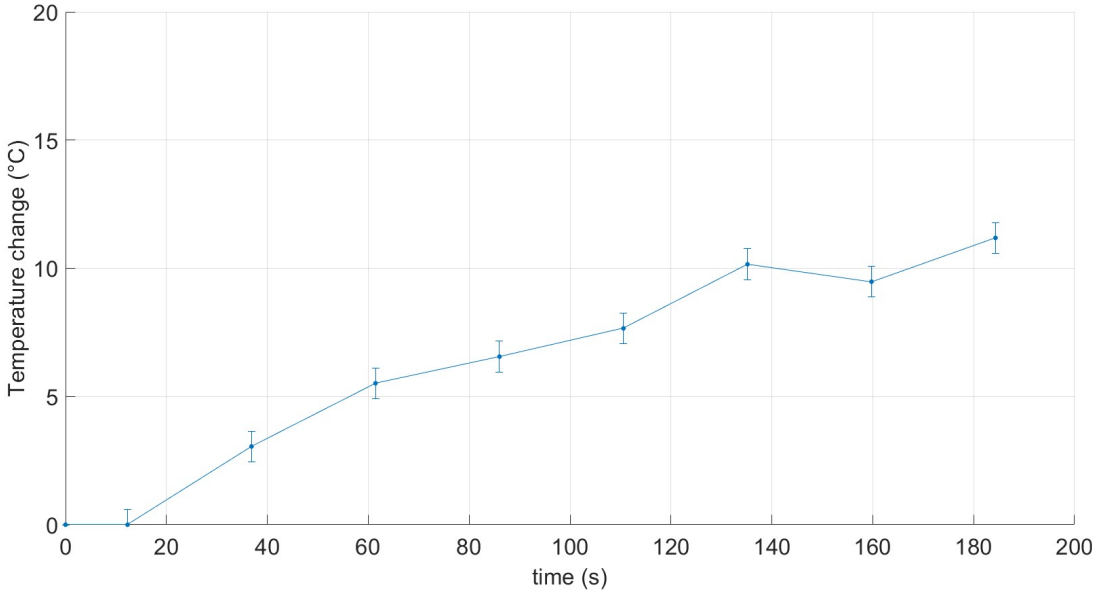

Fig. C.2: Real-time temperature graph reconstructed with 128 spokes for each frame.

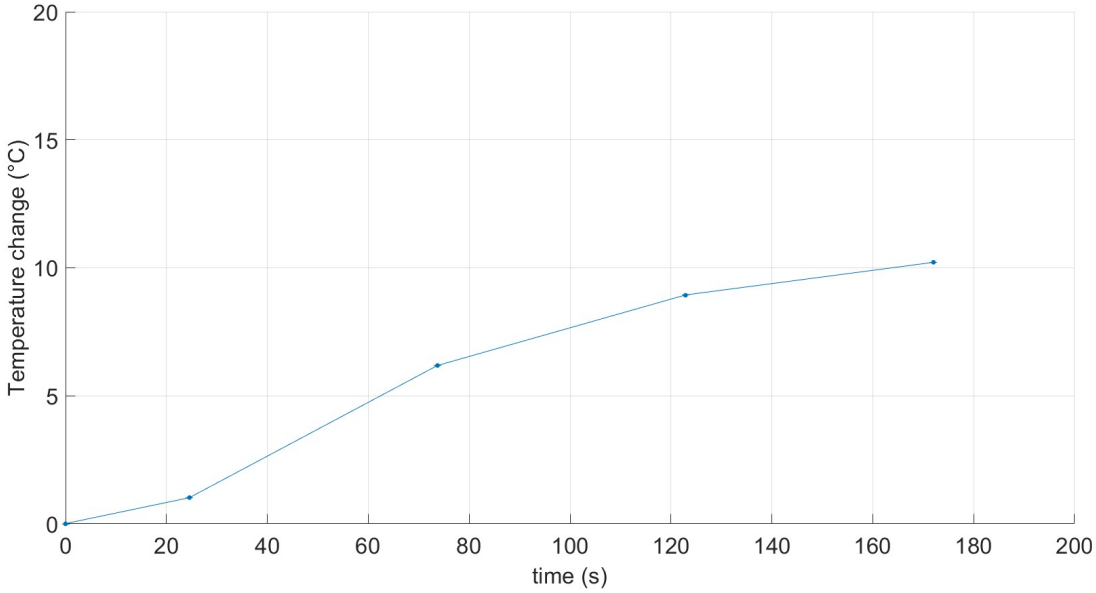

Fig. C.3: Real-time temperature graph reconstructed with 256 spokes for each frame.

D TEMPERATURE MAPS RECONSTRUCTED WITH MASKS

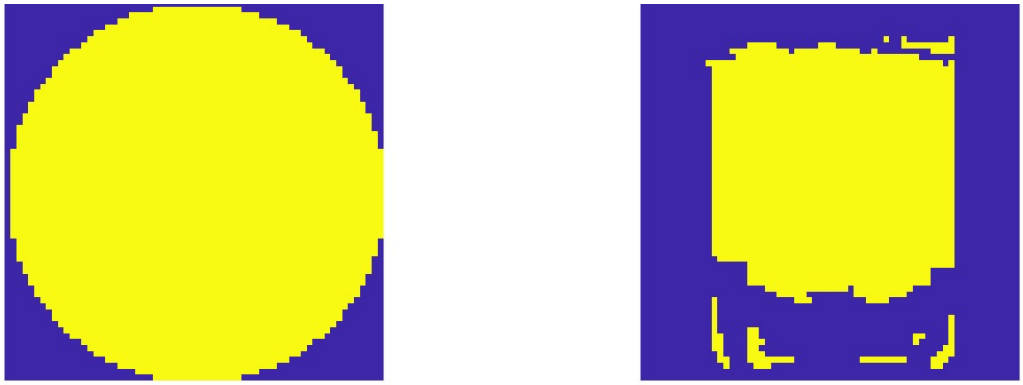

(a) Masker with size of radial FOV

(b) Mask of the phantom

Fig. D.1: Two masks used for image reconstruction with masks instead of oversampling

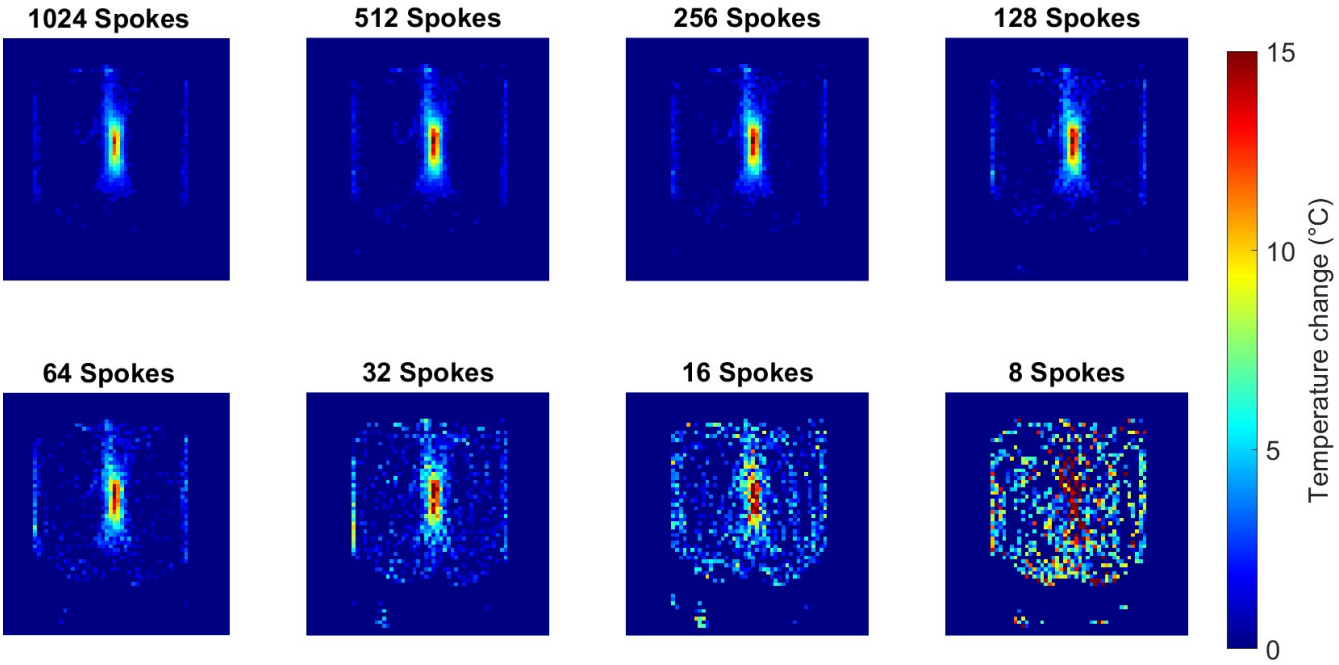

Fig. D.2: Temperature maps from data with different numbers of spokes reconstructed with the circular mask.

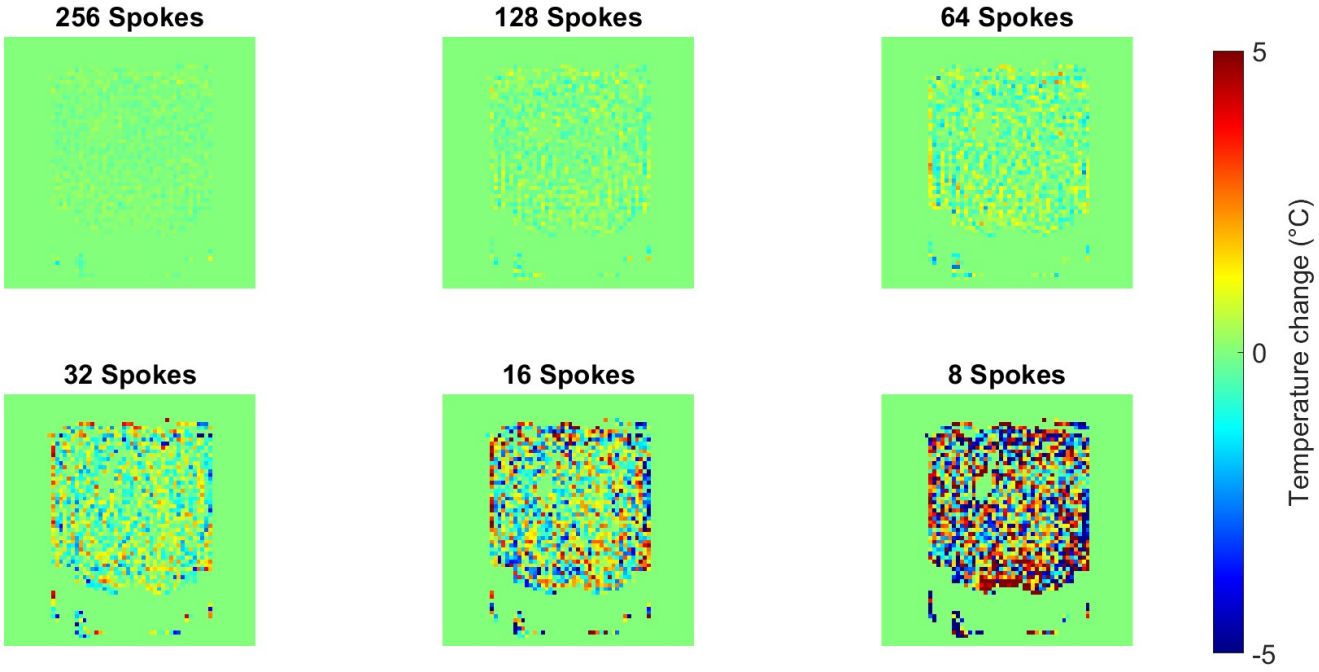

Fig. D.3: Temperature error maps reconstructed with the circular mask.

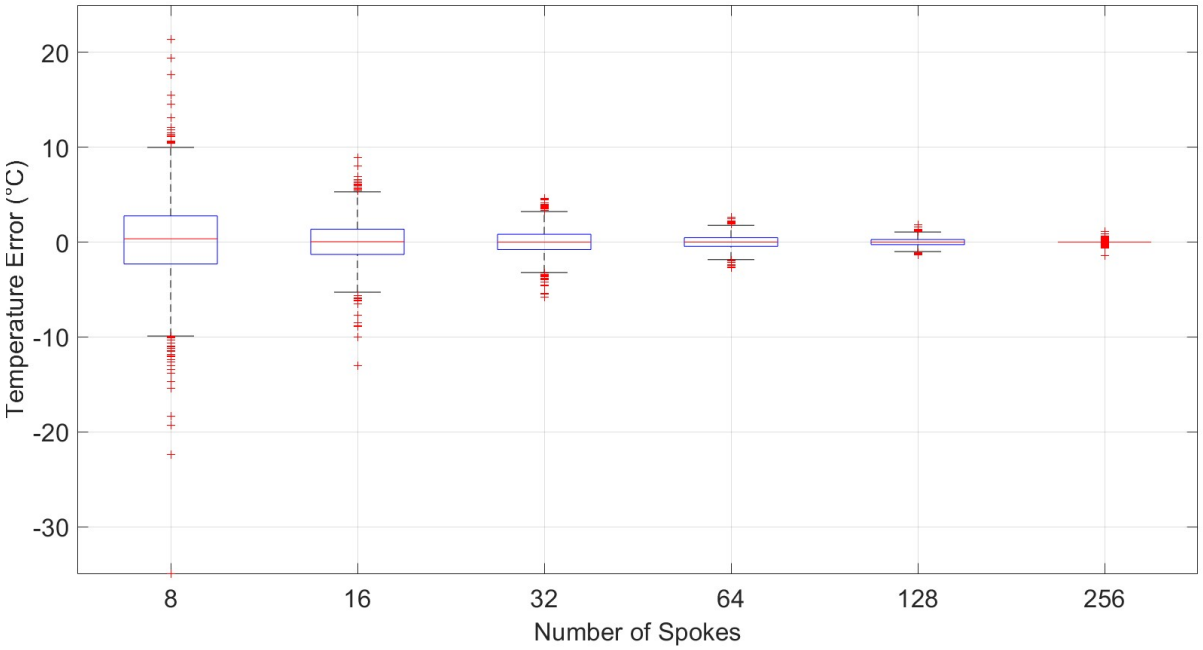

Fig. D.4: Boxplots of the temperature error of the circular mask reconstructions for different numbers of spokes.

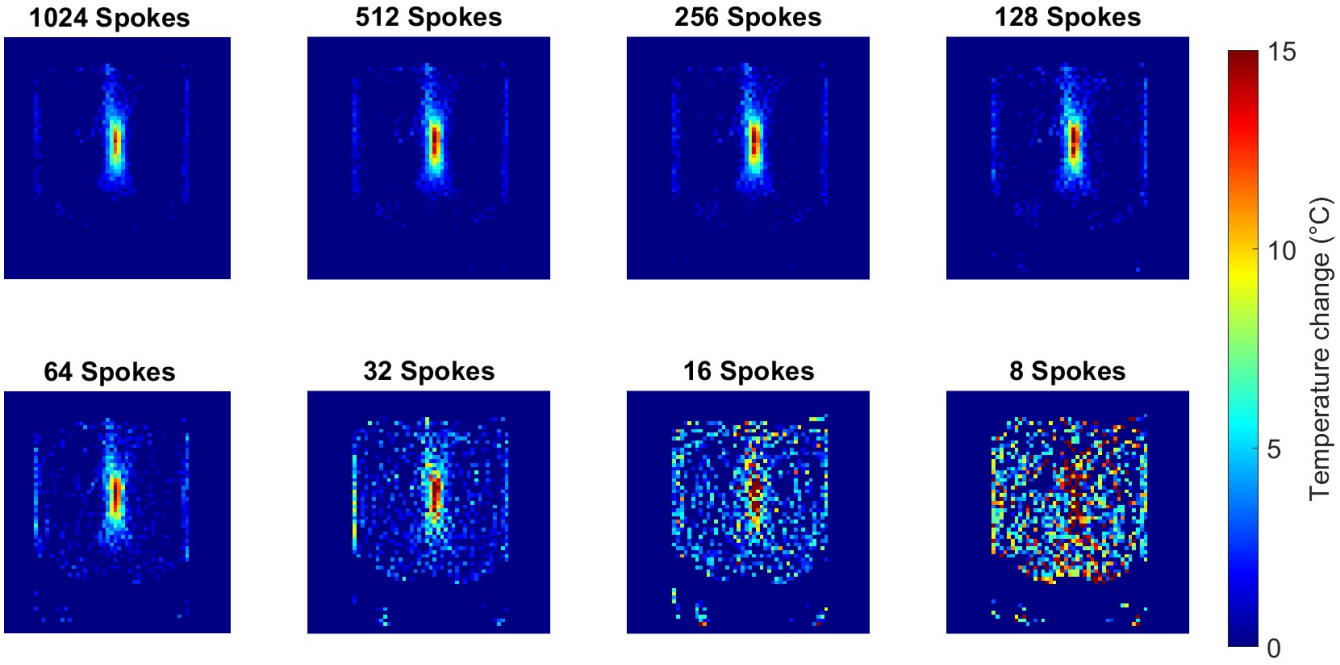

Fig. D.5: Temperature maps from data with different numbers of spokes reconstructed with the phantom mask.

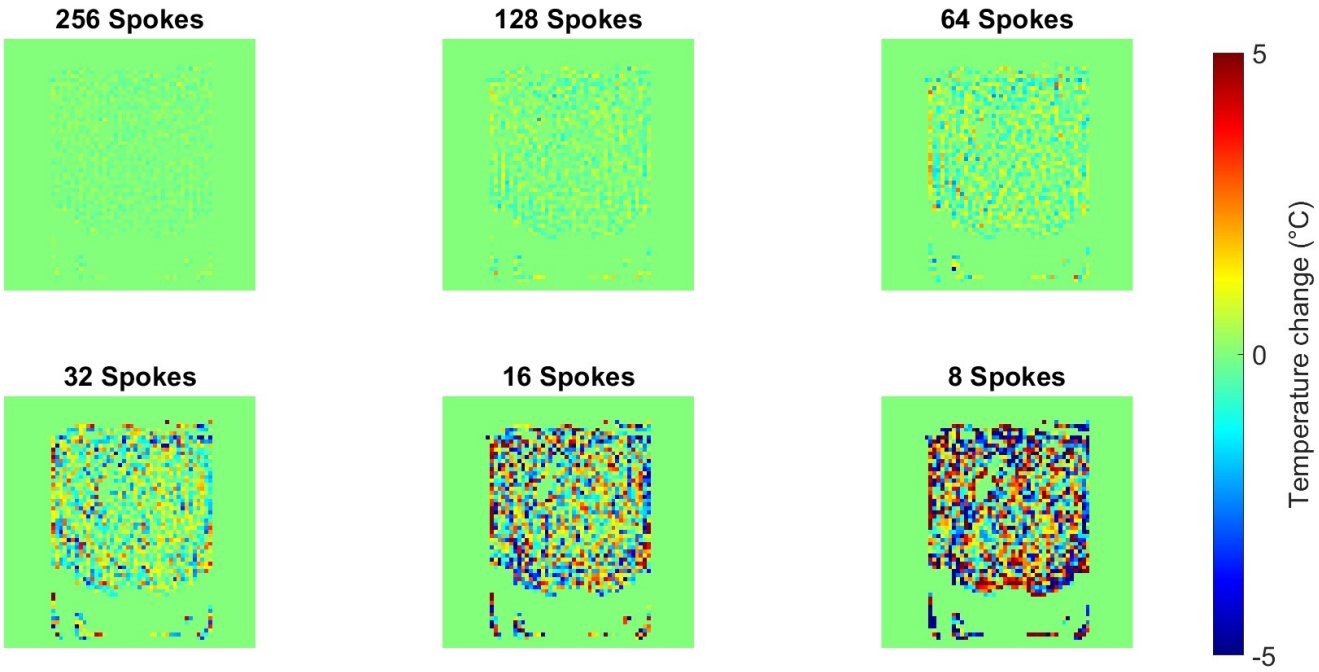

Fig. D.6: Temperature error maps reconstructed with the phantom mask.

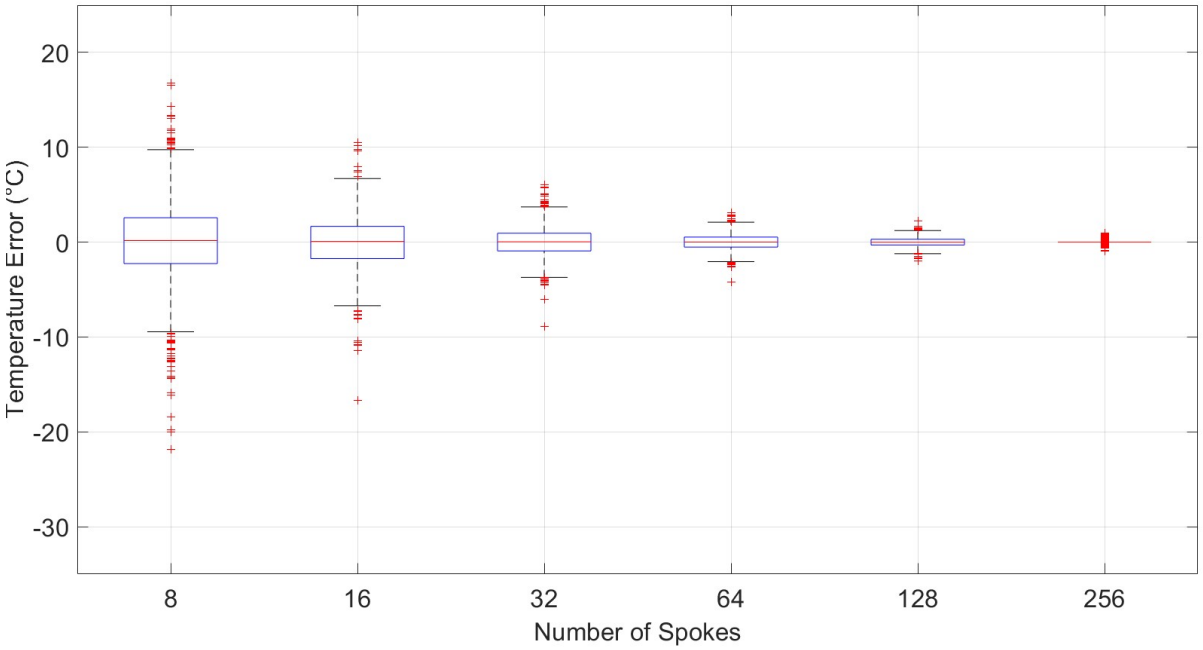

Fig. D.7: Boxplots of the temperature error of the phantom mask reconstructions for different numbers of spokes.